Article

Computational Estimation of Residence Time on Roniciclib and Its Derivatives against CDK2: Extending the Use of Classical and Enhanced Molecular Dynamics Simulations

Felipe Bravo-Moraga, Mauricio Bedoya,* Kirill Zinovjev, Iñaki Tuñon, and Jans Alzate-Morales*

Cite This: *ACS Omega* 2025, 10, 16731−16747

Read Online

ACCESS | 📊 Metrics & More | 📰 Article Recommendations | 🆂🇮 Supporting Information

ABSTRACT: Residence time is a crucial parameter for assessing the functional efficacy of drugs, quantifying the duration of a drug's binding to its target protein. It is directly related to therapeutic effects and the dosing regimen. Several factors can influence the residence time, including drug−protein binding kinetics and the unbinding pathways. Understanding the efficacy of a drug requires the characterization of both its binding kinetics and unbinding pathways from the drug−protein complex. By employing our previous computational protocol that uses enhanced sampling techniques such as well-tempered metadynamics (WT-MetaD) and classical molecular dynamics (cMD) simulations, it was possible to elucidate the inhibitor unbinding pathways and identify

molecular determinants that extend the residence time in a set of cyclin-dependent kinase 2 (CDK2) inhibitors. In this study, using WT-MetaD, the relative residence times of roniciclib and eight derivatives were quantified on the nanosecond timescale. Notably, substituting the R^5 position of the aminopyridine core with larger substituents significantly prolonged the computational residence time, which correlated well with experimental data ($R^2 = 0.83$). Our computational simulations reveal the critical importance of specific amino acids, including Phe80, Lys33, and Asp145, in maintaining the stability of the protein−inhibitor complex. These residues are key in keeping the hydration network around them, affecting the inhibitor binding duration. The hydrogen bond interaction between residue Asp145 and roniciclib and its derivatives is particularly noteworthy, significantly influencing the electrostatic contribution to the binding free energy when the halogen substituent size increases. Furthermore, our analysis of protein flexibility at the C-terminus and N-terminus angles revealed a relationship with the size of the R^5 substituent in the bound inhibitor, supported by principal component analysis. Additionally, different unbinding pathways were proposed, where it was found that inhibitors can dissociate from the CDK2 binding site through two principal routes: the α-helix D and β-1 and β-2 segments.
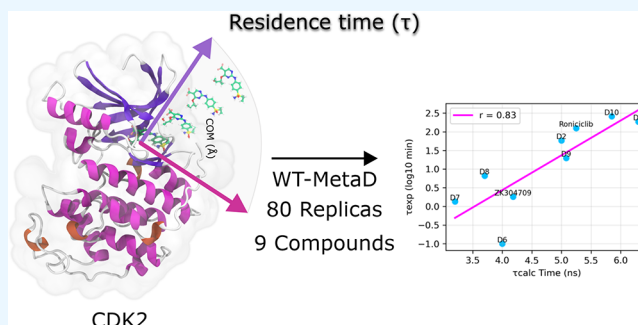
INTRODUCTION

CDK2 (cyclin-dependent kinase 2) is a member of the cyclin-dependent kinase family, which is composed of serine/threonine protein kinases that play a crucial role in various cellular processes. They actively regulate the cell cycle and the RNA polymerase II transcription cycle.[1] Proper CDK2 functioning is essential for maintaining cellular homeostasis. Aberrant activation of these enzymes can disrupt checkpoints and prevent the appropriate apoptotic responses. In contrast, their inactivation can restore those protein functions. This underscores their critical role in cellular regulation and integrity.[2,3] CDK2 controls the transition of phase G1 to S and plays a role in DNA replication. CDK2 can phosphorylate the retinoblastoma protein (Rb),[4] which binds to E2F transcription factors, causing their inhibition; this prevents the expression of genes that are necessary for DNA synthesis and progression, acting as a tumor suppressor, preventing excessive cell division.[5,6] To regulate these steps, CDK2 can form complexes with two cyclins, E and A, which activate the

CDK2, and once CDK2 is activated, it continues acting during the transition phases, facilitating DNA replication and cell progress.[7] Structurally (Figure 1), CDKs have a two-lobed structure, where the amino-terminal lobe contains β-sheets, while the carboxy-terminal lobe contains α-helices. The hydrophobic active site is located between these two lobes, connected by the hinge region ranging from residues 80 to 86, where the gatekeeper residue Phe80 in CDK2 is located. Another essential feature in protein kinases is the DFG motif, located in the activation loop and including residues Asp145, Phe146, and Gly147.[8,9] This motif is crucial in determining the different binding affinities and residence times (τ) of drugs,
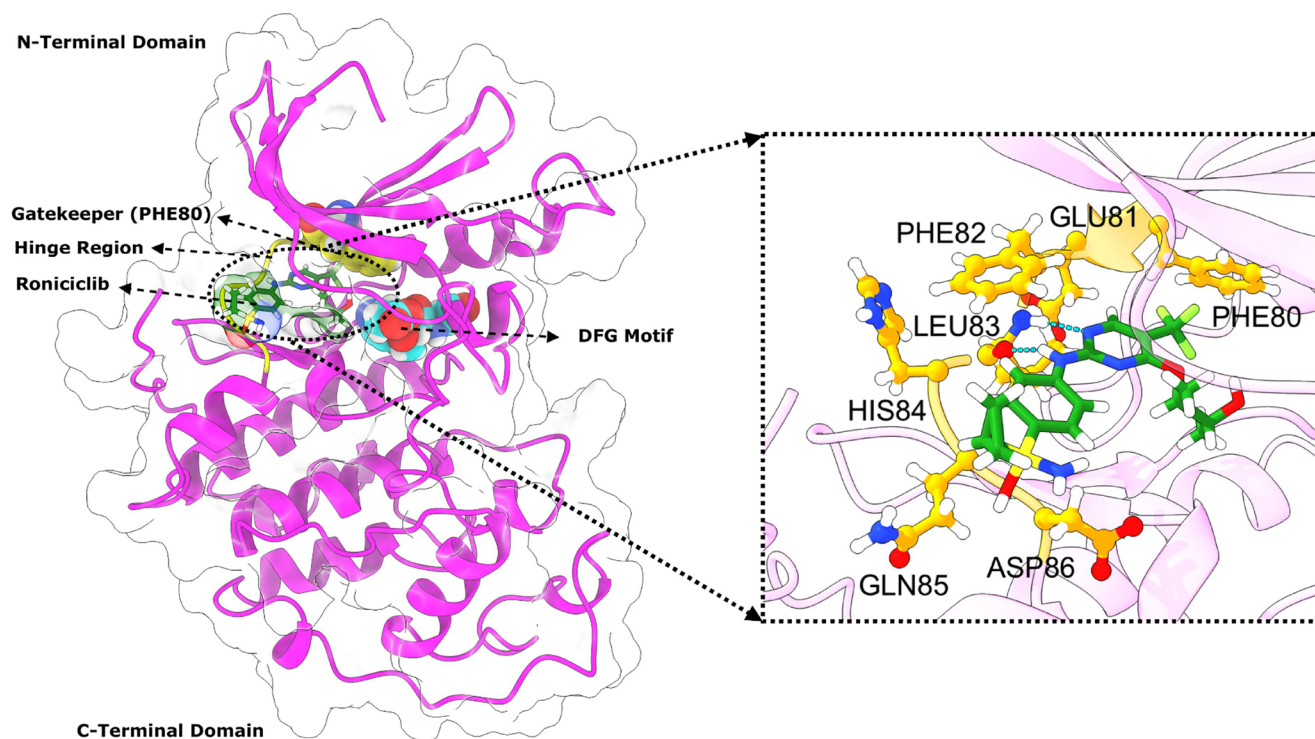
Figure 1. Structural features of CDK2 in complex with roniciclib (PDB ID 5IEV). The N-terminal domain predominantly comprises β-sheets, and the C-terminal domain is rich in α-helices. The structure includes several crucial regions: the DFG motif (shown in cyan) composed of residues Asp145, Phe146, and Gly147, the gatekeeper residue Phe80 (shown in yellow VdW), the ATP-binding pocket located between the N-terminal and C-terminal (shown in a green surface) where roniciclib is bound (green Licorice), and the hinge region, formed by residues Glu81 to Asp86, that connects the two lobes (shown in yellow). Close-up of the roniciclib (green) binding site and the hinge region residues that form hydrogen bonds and other interactions with it.

significantly depending on whether the inhibitors are classified as type I or type II. During binding, the DFG motif undergoes structural rearrangements and alternates between the DFG-in and DFG-out conformations.[1,10,11] Lys33 is a key amino acid that plays an essential role in binding kinetics and stability through hydrogen bonding and electrostatic interactions.

Phosphorylation and various cyclins and inhibitors regulate CDKs. Small-molecule inhibition of CDKs has been extensively investigated for cancer treatment, and several CDK inhibitors have advanced to phase II clinical trials.[12,13] One of these drugs is roniciclib (BAY 1000394) (Figure 1), a type I pan-CDK inhibitor with IC$_{50}$ values in the range of 5–25 nmol/L.[14] Roniciclib is characterized by its aminopyrimidine core, a common scaffold in kinase inhibitors essential for interacting with the ATP-binding site of CDKs with sulfoximine and trifluoromethyl substituents. Modifications at the R^5 position of the aminopyrimidine core, at the D-alaninol moiety, and the sulfoximine/sulfonamide group (see Table 1) significantly influence the inhibitor's binding kinetics and residence time. Here, we investigated derivatives ranging from the smallest substituent, hydrogen (H), to larger substituents, including halogens (F, Cl, and Br) and trifluoromethyl (CF$_3$). These structural modifications changed the hydration network, hydrogen bonding, and interactions with key residues at the active site and the hinge region, including the residues Phe80 and Asp145, which are essential for binding and residence time. The roniciclib derivatives include compounds with a hydrogen (H) atom, the smallest substituent, exhibiting the shortest residence time due to its inability to form stabilizing hydrophobic or electrostatic interactions with residues like Asp145 and Phe80. Fluorine

(F) atom, a slightly larger substituent than H, has a minimal improvement in τ, likely due to weak electronegativity and limited van der Waals interactions. Chlorine (Cl) atom is a halogen that enhances residence time by improving hydrophobic interactions and stabilizing the hydration network surrounding Phe80 and Asp145. Bromine (Br) atom is a bulkier substituent that increases τ through stronger hydrophobic and electrostatic interactions while inducing favorable protein conformational changes. The trifluoromethyl (CF$_3$) group, the largest substituent studied, significantly extended τ by maximizing hydrophobic interactions, restructuring the hydration network, and causing a conformation adaptation of the DFG (Asp-Phe-Gly) motif at the kinase. In addition to these R^5 modifications, variations in the side chain of D-alaninol moiety derivatives and sulfoximine/sulfonamide groups substantially influence the compound's potency and kinetics.

These drugs can inhibit cell proliferation at low nanomolar concentrations in a broad spectrum of human cancer cell lines.[15] Specifically, roniciclib is the result of the lead optimization of the aminopyrimidine ZK304709 by the incorporation of a sulfoximine, a trifluoromethyl (CF$_3$) group at the 5-position of the aminopyrimidine core, a replacement of NH by oxygen in the side chain (4-hydroxy pyrimidine instead of 4-aminopyrimidine), and a methyl group at the 4-position of the D-alaninol residue to give a secondary alcohol.[15] The ZK304709 is a multitarget drug that inhibits CDK1, 2, 4, 7, and 9, VEGF-R 1, 2, and 3, and PDGF-Rβ tyrosine kinases and inhibits the growth of pancreatic neuroendocrine tumors, acting over the cell cycle and angiogenesis. Ahmed et al. reported that phase I clinical trials evaluated the compound in

Table 1. Compound Identifiers, Chemical Structure, and Experimental Residence Times (τ) on CDK2

Compound ID	Chemical Structure	Reported residence time (τ, min)[14,15,19]	Compound ID	Chemical Structure	Reported residence time (τ, min)[14,15,19]
Roniciclib		124.61 +/- 24.11	D7		1.35 +/- 0.63
ZK304709		1.81 +/- 0.25	D8		6.62 +/- 1.73
D2		58.41 +/- 27.05	D9		19.82 +/- 4.16
D4		186.31 +/- 12.36	D10		258.65 +/- 78.62
D6		0.1 +/- 0.04			

patients with advanced solid tumors. The study enrolled 37 patients who received escalating doses (15−285 mg) of ZK304709 for 14 days, followed by a 14-day recovery period. Despite showing manageable side effects, the compound exhibited poor pharmacokinetic properties and limited therapeutic efficacy, ultimately leading to the discontinuation of its clinical development.[16−18]

Roniciclib has longer residence times on CDK2 and CDK9. The prolonged residence time on CDK2 is associated with a change in the hydration network near the 5-(trifluoromethyl)

group and the Phe80 gatekeeper residue. In addition, variations in the sulfonamide analogs at the aminopyrimidine 5-position (Table 1) by substituents with different electronegativities and nonpolar surface areas, such as 5-hydrogen (D6), 5-fluoro (D7), 5-chloro (D8), 5-bromo (D9), and 5-trifluoromethyl (D10), result in changes of three orders of magnitude in the residence time (τ) as shown by surface plasmon resonance (SPR) spectroscopy experiments ranging from 0.1, 1.35, 6.62, 19.82, and 258.65 min for each of the derivatives and 124.61 min for roniciclib (Table 1).[19] In addition, compounds of the

first generation, such as ZK304709 and analogs, were also considered for this study. These compounds include the ZK304709 with the Br substituent at the R^5 position and D2 and D4 with 5-(trifluoromethyl)-2-aminopyrimidine substitutions (Table 1) and different D-alaninol moiety patterns. These compounds have experimental residence times of short (1.81 min), medium (58.41 min), and long (186.31 min) durations, respectively.

Here, computational methods were used to determine the dissociation pathways of the CDK2 protein−ligand systems and the relative residence time of roniciclib and their halogen derivatives, ZK304709, D2, and D4 (Table 1), with a particular focus on variations at the R^5 position of the pyrimidine core. To do so, we applied a recent computational protocol, relying on computational simulations using conventional and enhanced molecular dynamics approaches that were previously tested and validated in similar protein−ligand systems like danusertib in complex with Aurora A and Aurora B.[20]

In the protein−ligand complex, kinetics depend on two rate constants: k_{on} that measures the association time of a protein−ligand complex and k_{off} that measures the dissociation time of a ligand from the target protein. Residence time is calculated as the inverse of the dissociation rate constant ($1/k_{off}$). Recently, residence time has been used as a reliable measure of drug efficacy under *in vivo* conditions instead of ΔG values.[21,22]

We aimed to elucidate the effect of the pyrimidine 5-substituent, D-alaninol, and sulfoximine/sulfonamide moieties on the residence time of roniciclib, ZK304709, and derivatives D2, D4, D6−D10. To achieve this, we performed several classical molecular dynamics (cMD) and well-tempered metadynamics (WT-MetaD) simulations. These approaches aimed to provide insights into the observed differences in experimental residence time and to elucidate the effects of the pyrimidine 5-substituent changes on residence time.[23,24] Moreover, enhanced sampling methods can be applied to study the drug binding and unbinding pathways from the protein.[25] With these methods, it is possible to explore the molecular determinants that regulate the binding and residence time of protein−drug complexes at the atomic level.[26,27] Metadynamics was used in a protocol to study the binding of ligands on the protein surface on the human nutrient deprivation autophagy factor-1 (NAF-1).[28] In more recent work, metadynamics was used to reveal the unbinding kinetics of the M3 muscarinic receptor, where the authors found that the method provides qualitative estimations of residence time and effectively captures the differences among ligands with short, medium, and long residence times.[29]

Four replicates of cMD simulations of 100 ns were performed for each of the complexes: CDK2−roniciclib, CDK2/D6, CDK2/D7, CDK2/D8, CDK2/D9, CDK2/D10, CDK2/D2, CDK2/D4, and CDK2/ZK304709. For each cMD simulation, 20 replicates of well-tempered metadynamics (WT-MetaD) were performed, resulting in 80 WT-MetaD replicates per protein−ligand system. This comprehensive approach was designed to measure the relative residence time and provide a molecular explanation and statistical significance for the experimentally observed differences in residence time.

Analysis of the cMD simulations highlighted the relevance of residue Asp145 within the DFG motif, which is conserved across all of the kinases. This residue revealed its importance in binding, as the size of the halogen substituent induces a conformational adaptation of the DFG motif, increasing the residence time through hydrogen bonds with the D-alaninol

chain.[19] Furthermore, the roles of Phe80 and Lys33 are described as well as their impact on changes in the hydration network of the protein active site and their contact with the different derivatives and roniciclib. In addition, the conformational changes of the protein in the presence of the derivatives and roniciclib were performed using angle variation analysis between two lobes and principal component analysis (PCA). These analyses corroborate the influence of substituent size on CDK2 protein stability and flexibility, where an increase in the size of the substituent is related to a prolonged experimental residence time.

WT-MetaD is an enhanced sampling technique used to characterize drugs' binding and unbinding path events and measure the free energy associated with these processes. This methodology has been proven to agree with experimental data.[30−33] In this work, relative residence times were measured on a nanosecond timescale by using the WT-MetaD method. These calculated residence times exhibited a strong correlation with the experimentally determined values. The Pearson correlation coefficient (R-square, R^2) of 0.83 indicates a robust relationship between the experimentally observed and computationally predicted relative residence times (τ). This finding reinforces the reliability of the WT-MetaD method in capturing the essential interactions that govern the observed differences in residence times based on substituent variations.

■ RESULTS AND DISCUSSION

Classical Molecular Dynamics Simulation Analysis. Four cMD simulations, each spanning 100 ns, were performed for the CDK2 system bound to derivatives D6−D10, roniciclib (BAY 1000394), D2, D4, and ZK304709. The root-mean-square deviation (RMSD) was evaluated using the backbone atoms of CDK2 (Figure 2A) to assess the stability of the protein−ligand systems. The RMSD fluctuated between 2 and 3 Å for CDK2 bound to derivatives D7, D8, D9, and D10, as well as for roniciclib and ZK304709, and was approximately 3.5 Å for the system involving D6, D2, and D4. Notably, CDK2 bound to different compounds showed high stability over the last 60 ns of the simulation. The RMSD shows that CDK2 is more stable according to the size of the derivatives, whereas derivative D10 has less variation in the RMSD of the protein backbone, indicating a relatively stable behavior. Derivatives D6, D2, and D4 show a more significant variation in the RMSD of the protein backbone, indicating more structural fluctuations during the simulation. For the remaining derivatives, the RMSD fluctuations follow a pattern from significant fluctuations to less variability. This trend correlates with the size of the substituent group.

When roniciclib and all derivatives were analyzed, they exhibited stability throughout the 100 ns simulation time with minimal fluctuations in the RMSD values. However, an exception was noted for derivatives D6 and ZK304709, where the RMSD increased from 1 to approximately 1.7 Å. The deviation in RMSD of derivative D6 can be attributed to a subtle change in the position of the ligand within the active site in the simulations (Figure 3).

Analysis of CDK2 bound to roniciclib and derivatives showed that the compounds form hydrogen bonding (HB) interactions with hinge region residues. A consistent pattern of interaction involving residues within the hinge region spans residues 80−86. The primary HB interactions of derivatives and roniciclib with CDK2 are shown in Figure 4. For D6 (Figure 4A), the backbone oxygens of Phe82, Leu83, and
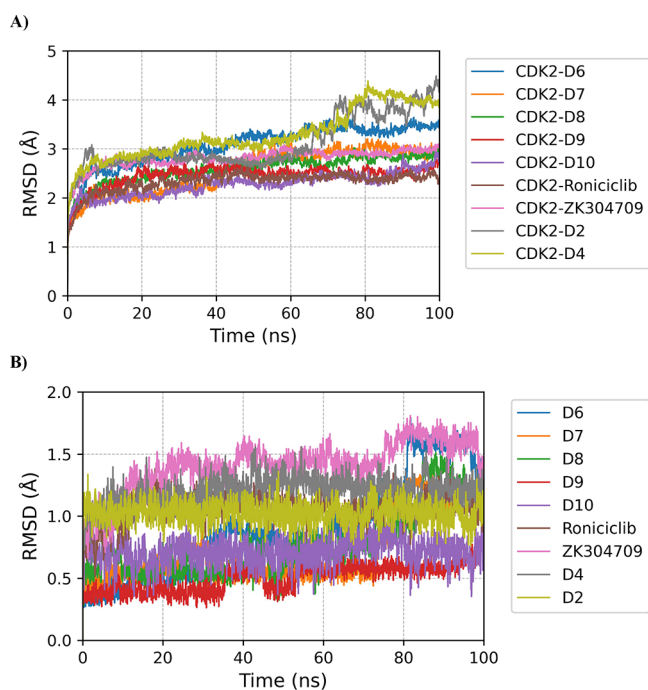
A)

B)

Figure 2. RMSD analysis of CDK2 bound to roniciclib and its derivatives. (A) RMSD of the CDK2 backbone, illustrating stability over four replicates of 100 ns in the presence of different derivatives D6−D10, roniciclib, D2, D4, and ZK304709. (B) RMSD of roniciclib and derivatives, highlighting stability over the four replicates during 100 ns of molecular dynamics simulations.
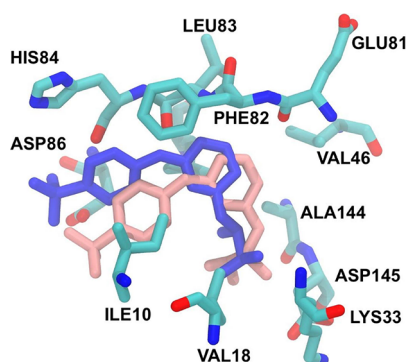

Figure 3. Derivative D6 in the active site of CDK2. The variation in root-mean-square deviation (RMSD) of D6, along with the cMD simulations, is attributed to its change in position within the active site. In the simulation, pale red corresponds to the initial position, while blue represents the final position.

His84 form HB interactions as well as an interaction between a water molecule and the nitrogen of the aminobutanol chain. For D7 (Figure 4B), HB interactions were detected with the backbone oxygen of residues Phe82, Leu83, and Glu81, along with Asp86. For D8 (Figure 4C), HB interactions were identified with the oxygen and hydrogen atoms of the backbone of Phe82 and Leu83 and an aromatic H-bond with the oxygen backbone of Glu81. For D9 (Figure 4D), hydrogen bond and aromatic H-bond interactions were observed with the backbone of Phe82 and Leu83, along with an aromatic H-bond with the oxygen backbone of Glu81. For D10 (Figure 4E), HBs and aromatic H-bond interactions were found with the oxygen and hydrogen atoms of the backbone of Phe82 and Leu83, with an additional aromatic H-bond formed with

Glu81. In roniciclib, an H-bond interaction was observed between the oxygen atom of Leu83 and the amine backbone of Phe82, with an additional aromatic H-bond formed with the oxygen backbone of His84, Gln85, and Glu81. For derivatives D2 and D4, an H-bond interaction was observed between the oxygen atom of Leu83 and the amine backbone of Phe82 (Figure 4G,H). Finally, in the compound ZK304709 were observed H-bond interactions with Phe82 and Lys33 (Figure 4I).

The gatekeeper residue is a critical amino acid in the hinge region of protein kinases (Phe80 in CKD2). This residue plays an essential role in the active site of kinases for the development of the inhibitors, as it can open the active site to a hydrophobic back pocket in the kinases. Phe80 is located near the ATP-binding site and is a key structural element that interacts with inhibitors such as roniciclib and its derivatives in CDK2. The percentage of contacts for each derivative with Phe80 increases as the size of the atoms changes from hydrogen (H) to halogens (F, Cl, and Br) and trifluoromethyl (CF_3). Notably, the R^5 substituent has a majority of the contacts. Specifically, for D6−D10, the percentages of contacts are 26.1, 19, 24.9, 29.7, and 26.4%, respectively. For D2 and D4, they are 17.1 and 19.3%, respectively, and for ZK304709, it is 17.1% (Figure S43). The dynamics of protein and conformational changes occurring upon ligand binding can be assessed using a method based on principal component analysis (PCA), where the cumulative variance of the 10 PCAs shows that the main contributions are made by the four first components representing over 50% of the variance of the data for each complex (Figure S45). This analysis was employed to measure the fluctuations of CDK2 in the presence of various derivatives and roniciclib. Analysis of CDK2 bound to roniciclib and its derivatives yielded insights about the conformational dynamics of CDK2. For D6 (Figure S44A), we observed three primary states in the conformational space. However, the CDK2 motions showed extensive structural fluctuations and were more extended. This was indicated by conformational changes and reduced stability during binding, as evidenced by the PC1 and PC2. D7 (Figure S44B) presented three principal local minima, which were closely located, suggesting a more compact structure. For derivatives D6 and D7, proteins PCA1 and PCA2 were less stable and had fewer populated states. D8 (Figure S44C) displayed three large populated states. Three primary conformational states were observed for D9 (Figure S44D). The distinct conformations were densely populated and had separated states. D10 (Figure S44E) had a marked primary population state, indicating the strong compactness of the structure of the derivative. This behavior was similar for roniciclib (Figure S44F), where we observed a leading population state and two less populated states. For derivatives D2 and D4 (Figure S44G,H), we observed two localized main minima along PC1 and PC2 with many population states. In contrast, we observed only one minimum in ZK304709 (Figure S44I), which is more spread along PC1 and PC2.

The local movements of a protein analyzed by principal component analysis (PCA) can be correlated to the angle analysis of the C-terminal and N-terminal lobes of CDK2. This correlation is evident by the dotted product angle formed between two vectors. The first vector is formed by the center of mass (COM) of α carbon (CA) atoms of residues 181−198 at the α-helix segment, and the second vector is formed by the COM of CA atoms of residues 4−23 located at the beta 1 and
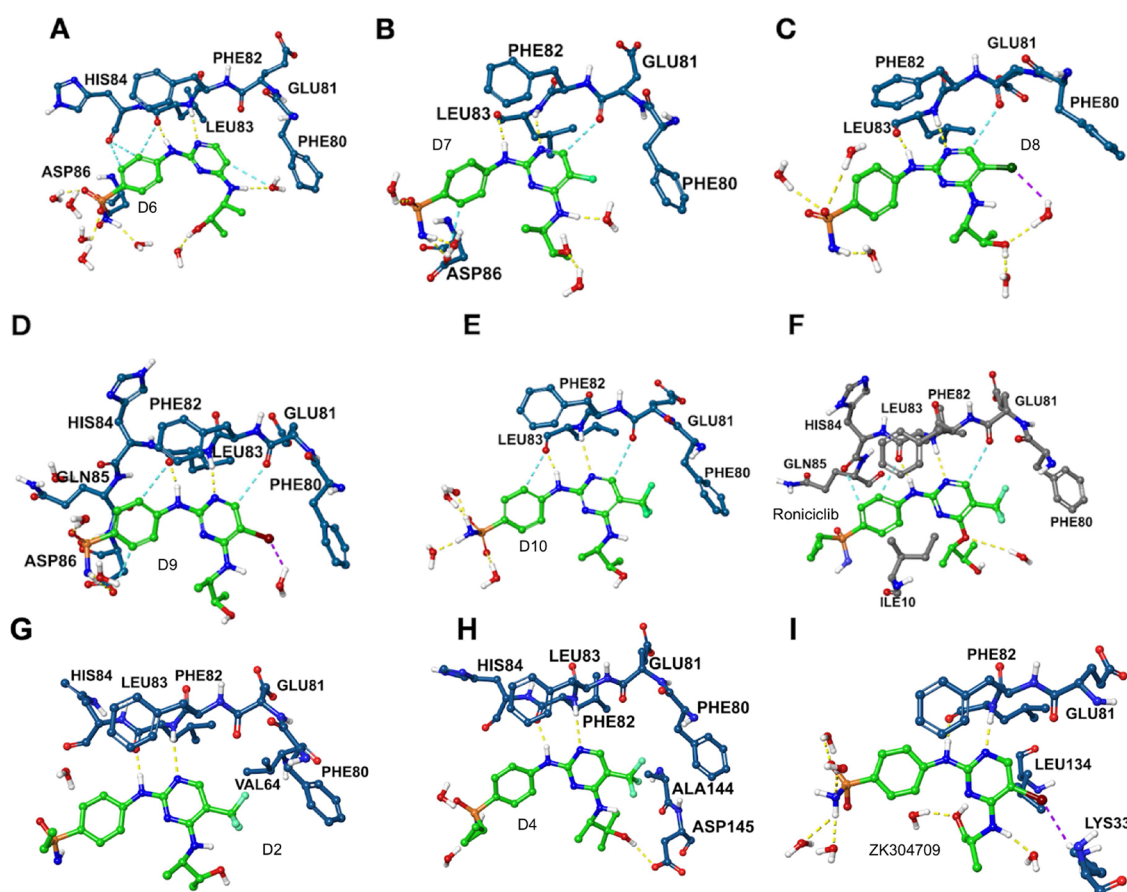
Figure 4. Structures of all derivatives and roniciclib bound to CDK2 at a distance of 3 Å. The main HBs are depicted as yellow and white dashed lines for polar and nonpolar HBs. (A) D6, (B) D7, (C) D8, (D) D9, (E) D10, (F) roniciclib, (G) D2, (H) D4, and (I) compound ZK304709.
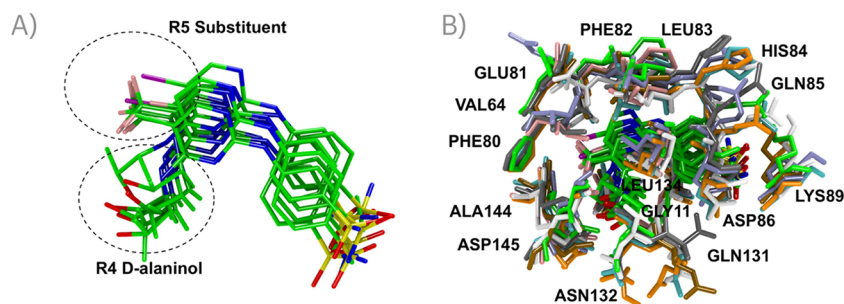

Figure 5. Residue interaction of all derivatives and orientation of the R^5 substituent and R^4 aminobutanol in the active site. (A) Ligand orientation in the active site for derivatives in the R^5 substituent: derivatives D7 (F cyan color atom), D8 (Cl green color atom), D9 (Br, purple color atom), and D10 ($-CF_3$ cyan color atom); the aminobutanol is oriented differently in comparison with D6, where aminobutanol is flipped. (B) Interaction between the derivatives D6, D7, D8, D9, and D10 and the additional residues ASN132, GLN131, GLY11, and ILE10 that interact with the derivatives D7, D9, and D10. Ice blue amino acids for derivative D6, brown amino acids for D7, white amino acids for D8, green amino acids for D9, and cyan color for D10. Gray amino acids are for D2, orange amino acids are for D4, and pink amino acids are for compound ZK304709.

2 segment. When CDK2 is bound to derivative D6, the angle between the lobes is more open throughout the cMD simulation than for other derivatives. The angle analysis (Figure S46) reveals that derivative D6 impacts the lobe opening with an average angle of 22.54° between the two lobes. On the other hand, derivatives D7, D8, D9, and D10 show angles of 32.74, 32.74, 16.54, and 16.12°, respectively, while CDK2 bound to roniciclib shows an average angle of 17.83°. The angles measured for D2, D4, and ZK304709 were 18.23, 24.29, and 22.25°, respectively. The angle evolution over time (Figure S46) suggests that all derivatives and complexes remain stable over the 100 ns simulation, and

changes in the angle degree are observed for complexes with higher residence time.

This analysis suggests that as the size of the substituent increases, the angle formed between the two lobes becomes closed, indicating the compactness of the proteins for the large-size derivatives. This compactness of the protein could hinder the exit of the ligand, causing the ligand to remain in the active site for a longer time and increasing the residence time for these derivatives and roniciclib. Consequently, the enzyme must adopt a more open conformation between the lobes to facilitate the exit of the ligand, as evidenced by the angles of derivatives D6 and D7.

Furthermore, substitution at the R^5 position triggers an adjustment in the orientation of the aminobutanol moiety located at the R^4 position of the pyrimidine core (Figure 5A). This behavior is determined by the size of the substituents present in each of the derivatives, which elongate the aminobutanol chain in all derivatives except for the hydrogen derivative, D6, wherein the ligand adopts a distinct conformation that orients the aminobutanol chain toward Phe80. In contrast, this chain aligns toward the activation loop zone in other derivatives (D7, D8, D9, D10, D2, and D4). Consequently, this reorientation promotes interactions between the aminobutanol chain and additional residues of the active site, not seen in derivative D6, particularly with residues Gln131 and Asn132 for derivatives D7, D8, D9, and D10. Interactions with residues Ile10 and Gly11 of the β-1 and β-2 zones are also observed in derivatives D7, D9, and D10 (Figure 5B). The increase in residue interactions is consistent with the size of the R^5 substituent and correlates with the reported experimental residence time for the derivatives. The D2, D4, and ZK304709 contacts are similar to derivative D10 because the ligands have −CF$_3$ and −Br substitutions.

To obtain more structural and molecular information about the binding mode of the derivatives and roniciclib to CDK2, the number of HBs between the different derivatives was calculated by using the hbond module of cpptraj of AmberTools22. The hydrogen bond interactions between the protein and derivatives were measured throughout the cMD simulations using default parameters: a donor−acceptor distance cutoff of 0−3.0 Å and a donor−hydrogen−acceptor angle greater than 135°. Derivatives exhibiting lower residence times, such as D6 and D7, displayed an average HB percentage below 5%. Conversely, derivatives with extended residence times, such as D8, showed a significantly higher average HB percentage, approaching 30%. This trend was consistent with derivatives D9 and D10, which maintained an average HB percentage exceeding 40% during the simulations. The derivatives D2, D4, and ZK304709 showed a significantly higher average HB percentage, over 79% for D2, 85% for D4, and 65% for the compound ZK304709. This follows the trend where compounds with a lower experimental residence time have lower HB percentages (Figure 6).
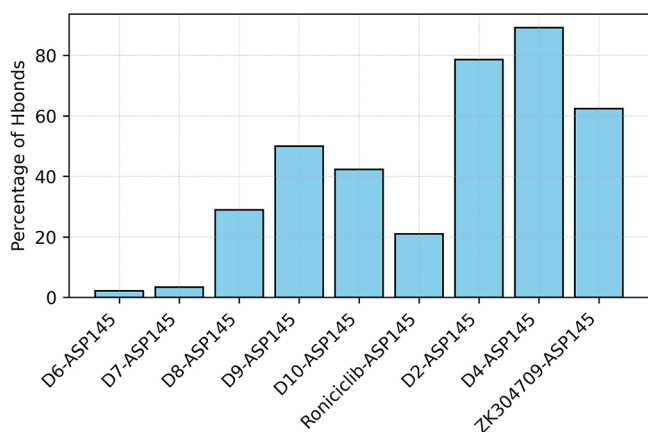

Figure 6. Hydrogen bonds between Asp145 and roniciclib and derivatives. Percentage of hydrogen bond interaction along all molecular dynamics simulations of derivatives D6−D10, roniciclib, D2, D4, and ZK304709 with the residue of Asp145.

Interestingly, the number of HBs of derivatives with Asp145 corresponds to the residence time observed for the different inhibitors according to the size of the substituent group. This is due to the ligand adopting a distinct conformation in the active site, orienting its aminobutanol chain to the Asp145 residue to form HBs with the carboxyl group of this residue.

In the 100 ns cMD simulations, the energetic contribution of each residue to the binding free energy was analyzed for each derivative. The analysis revealed that the electrostatic contribution to binding is more pronounced in the hinge region residues, specifically Glu81, Phe82, and Leu83, across all derivatives.

Key amino acids for the binding of roniciclib and its derivatives are located in the DFG motif. In particular, the analysis reveals that the residue Asp145 plays a significant role in binding all derivatives, as confirmed by our cMD analysis using the LIE (Figure 7) approach, the MM/GBSA method (Figure S1), and experimental data reported by other authors.[19]

An increase in the electrostatic contribution of Asp145 to the binding correlates well with the size variation of the substituent in R^5. For instance, the electrostatic contribution of Asp145 in derivative D6 is −2.5 kcal/mol and for D7 is −2 kcal/mol. However, a notable increase is observed in derivative D8, where it exceeds −9.2 kcal/mol. Derivatives D9 and D10 exhibit even higher contributions of −13.0 and −12.1 kcal/mol, respectively. In the case of roniciclib, the contribution of residue Asp145 to binding is −6.9 kcal/mol. Similar to the rest of the derivatives with high residence time, derivatives D2 and D4 exhibit higher electrostatic contributions for Asp145, of −17.9 and −15.8 kcal/mol, respectively, while compound ZK304709 has a lower contribution of −5.6 kcal/mol, similar to the compound with a lower residence time (Figure 7).

Remarkably, the substantial energetic contributions of derivatives with Asp145 align with those of derivatives having a larger R^5 substituent. This correspondence between the energetic contributions of Asp145 and the substituent size is notably consistent with the experimentally reported residence times for each derivative and roniciclib, as detailed in the study by Ayaz et al.[19]

Changes in the size of the substituents at the R^5 position and the electronegativity of the halogens led to changes in the hydration network near the DFG motif and Phe80 within the binding zone. These changes can explain the variations in the electrostatic contributions of each derivative with Asp145, particularly when considering the hydration environment around Asp145 and the hydrogen bonding interactions (Figure 8). Specifically, in the case of derivative D6, the interaction with Asp145 involves a water molecule mediating an HB between the hydroxyl group of D6 and the carboxyl group of Asp145. In addition, the amine group of Lys33 forms HB with the same water molecule.

For D7, a water-bridge is formed between the hydroxyl group of the derivative and the carboxyl group of Asp145. The same water molecule also interacts through a hydrogen bond with the amino group of Lys33. Moreover, a salt bridge is formed between Asp145 and Lys33 in D7.

Derivatives D8, D9, and D10 exhibit a different mode of interaction compared to that of D6, where the hydroxyl group of the aminobutanol chain forms a direct hydrogen bond with the carboxyl group of Asp145. This direct HB implies more intimate and specific binding between the derivatives and the
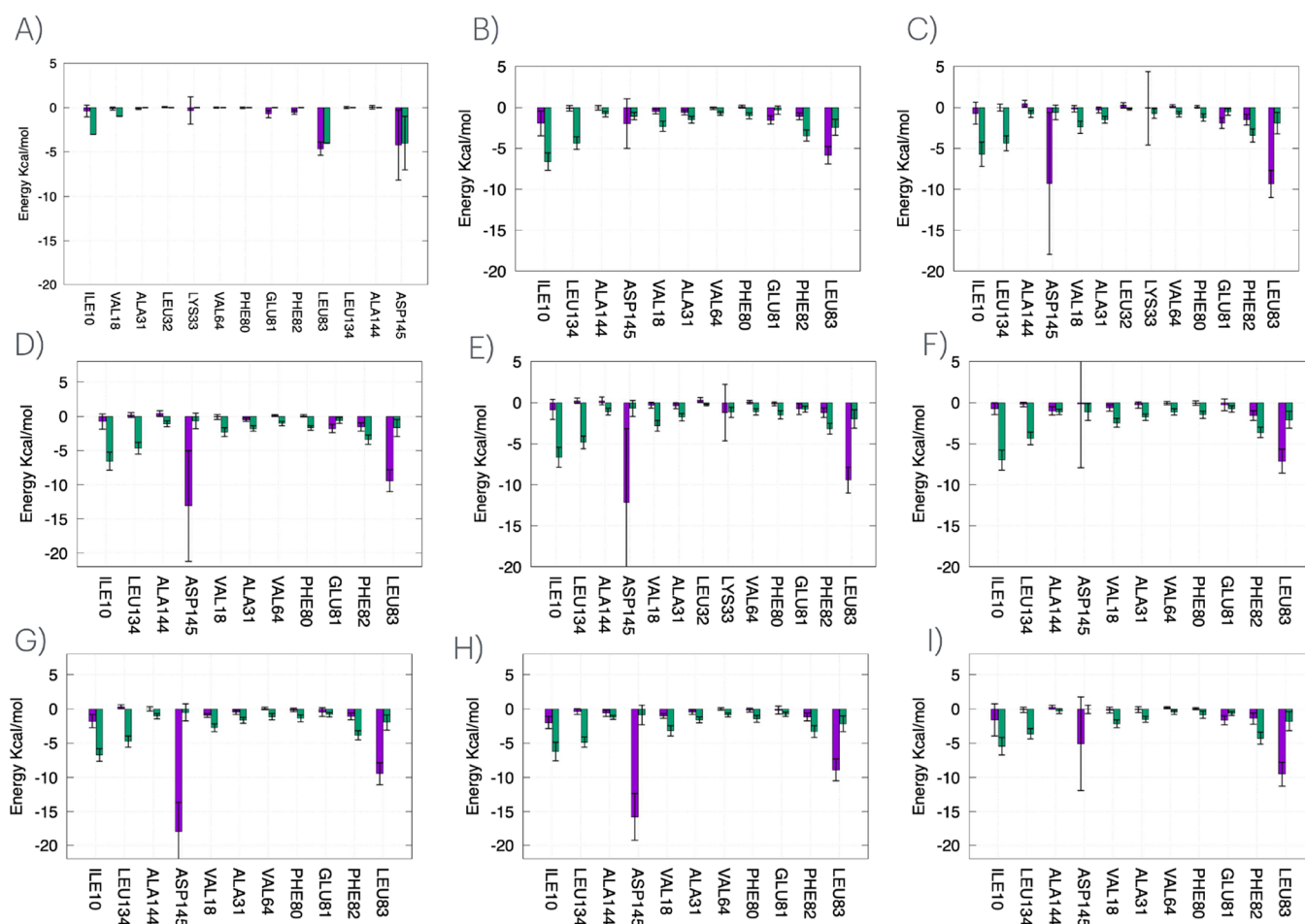
Figure 7. Electrostatic (purple) and van der Waals (green) contribution per residue of the active site of CDK2 with each of the derivatives D6–D10 (A–E), roniciclib (F), D2 (G), D4 (H), and ZK304709 (I). One of the essential residues is Asp145, with a high electrostatic contribution for derivatives D8, D9, D10, roniciclib, D2, and D4. The binding free energy and its contributions were calculated by using the LIE method.

Asp145 residue. Moreover, a consistent salt bridge between Asp145 and Lys33 is maintained across these derivatives.

For roniciclib, the interaction with Asp145 is facilitated by direct HB between the hydroxyl group of roniciclib and the carboxyl group of Asp145. Additionally, two hydrogen bond interactions occur between the amino group of Lys33 and roniciclib: one with the ether oxygen and another with the hydroxyl group. There is also a salt bridge interaction between the amino group of Lys33 and the carboxyl group of Asp145.

For derivatives D2, D4, and ZK304709, the aminobutanol chain forms a direct HB with the carboxyl group of Asp145; in addition to this hydrogen bond interaction, Lys33 can make a salt bridge with Asp145 in derivatives D2 and D4.

The stabilization of the inhibitor−CDK2 complex and its interactions depend significantly on the role of residues Lys33 and Phe80. These residues influence the inhibitor's binding affinity and residence time on the target protein. Moreover, their interactions with inhibitors such as roniciclib and analogs are crucial for the complex's formation, stability, and residence time. In particular, variations in the hydration network further affect these interactions. The water shell module of cpptraj was used to calculate the water shell around the residues. The default cutoff distance parameters for the first and second water shells were 3.4 and 5.0 Å from the COM of the residues, respectively, and the mask is the selection of all atoms of residues Lys33 and Phe80. An analysis that counts the number

of water molecules around this residue shows the rearrangement of the hydration network. A comparison was performed between the derivative D10 with the −CF$_3$ substituent, where the residence time is longer, and the derivative D6 with the hydrogen substituent, where the residence time is lower. For instance, as the size of the halogen substituent groups increases, the average water shell around Lys33 decreases, suggesting the displacement of water molecules in the active site and correlating with increased residence time. Specifically, for derivatives such as D6, D8, and D10, the average number of water molecules around Lys33 decreases almost progressively: 17.22, 9.03, and 9.31, respectively (Figure 9A). Moreover, Phe80 modifies the hydration network induced by the halogen substituent, which can alter the protein's conformational dynamics and significantly impact the residence time.[19] Phe80 shows that the average water molecules for derivatives D6 and D10 are 6.97 and 6.01, respectively. This suggests that the halogen group changes the hydration network and the number of water molecules around the substituents (Figure 9B).

Relative Residence Time of Derivatives of Roniciclib with WT-MetaD. The relative residence times of roniciclib and its derivatives were assessed by using 80 samples of WT-MetaD simulations for each complex CDK2−inhibitor. Starting from the final steps of each of the four independent classical molecular dynamics trajectories (Traj1−Traj4), 20
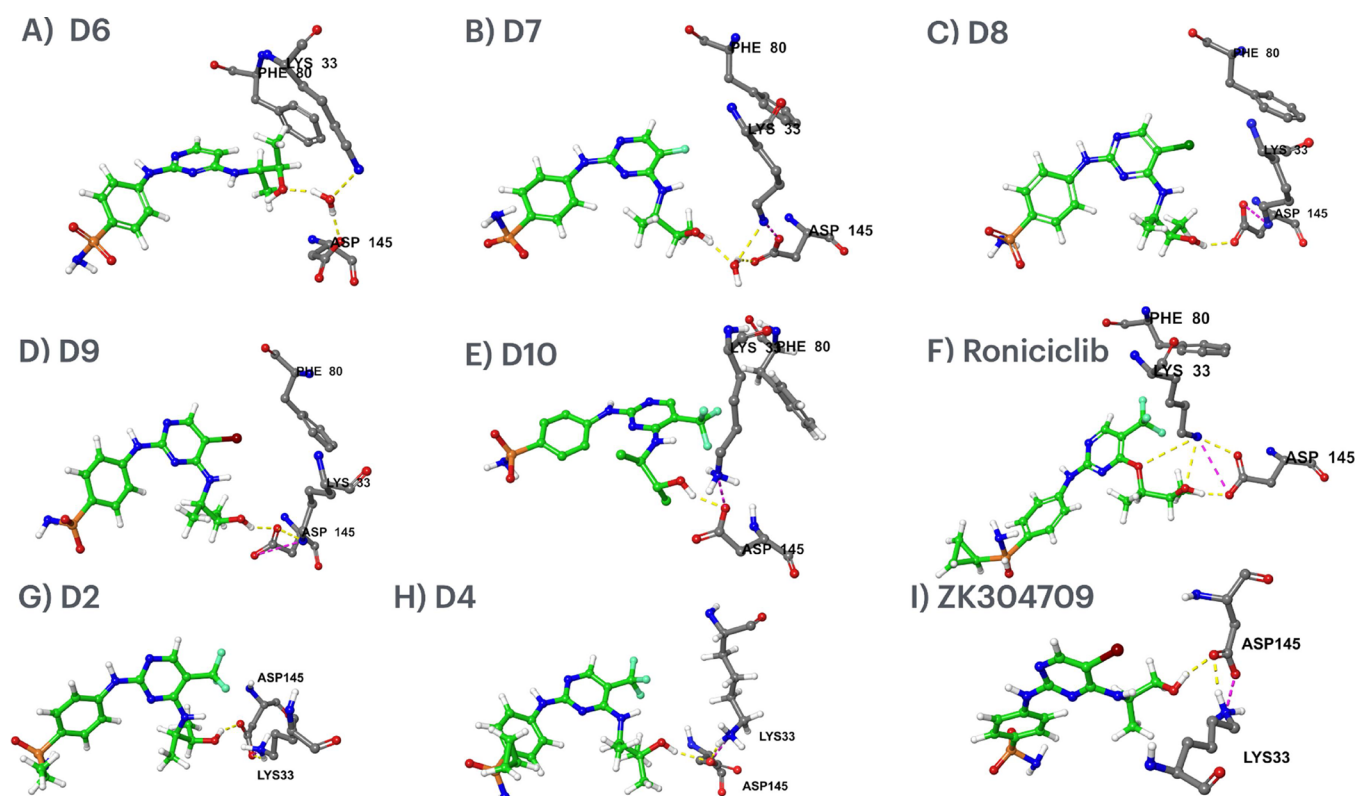
Figure 8. Hydrogen bond interaction of all derivatives with residues Asp145 and Lys33 is shown as yellow lines. For derivatives D6 and D7, where the substituents are H and F, a water molecule mediates the interaction with Asp145. In derivatives D8, D9, D10, and Roniciclib, the interaction with the aminobutanol is via a direct HB with Asp145. Derivatives D2, D4, and ZK304709 form HB interactions with Asp145 and additional salt bridges (magenta lines) between Lys33 and Asp145.
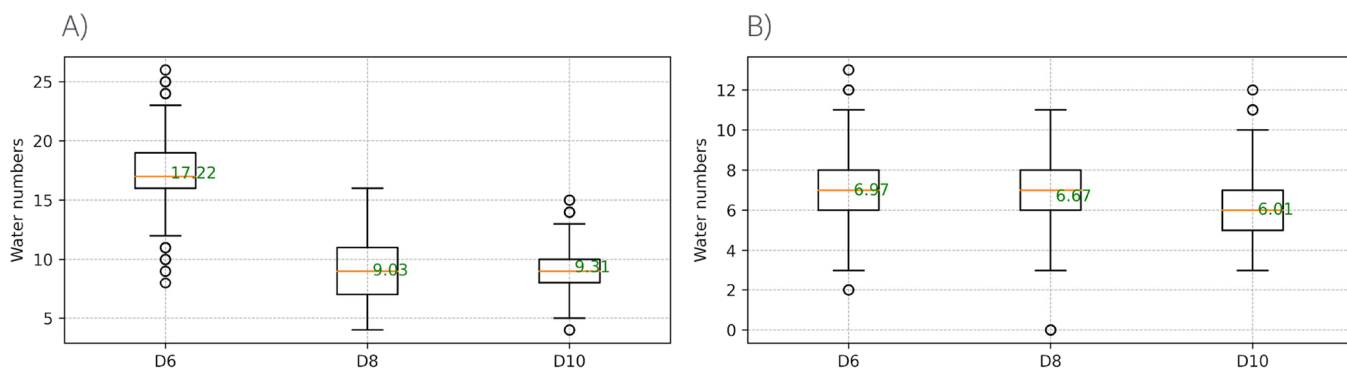

Figure 9. Average water shell molecules around Lys33 and Phe80. (A) Average water shell around 5 Å of residues Lys33 and (B) Phe80. For D6 with R^5 hydrogen, D8 with −Cl, and D10 with −CF$_3$.
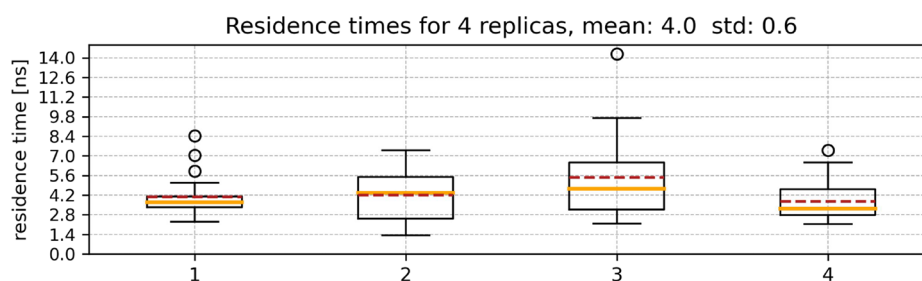

Figure 10. Box plot of relative residence times given in nanoseconds (ns) for the D6/CDK2 complex. The averages of the four trajectories, each with 20 replicates, are shown in the box plots. The whisker shows the range of the data; the median is in orange, the mean is in red dashed lines, and the outliers are in circles.

Figure 11. Box plot of relative residence times in nanoseconds (ns) for the D10/CDK2 complex. The averages of the four trajectories, 1−4, with 20 replicates each, are shown in the box plots. The whisker shows the range of the data; the median is in orange, the mean is in red dashed lines, and the outliers are in circles. For this derivative, we found two outliers in Traj3 and Traj4.
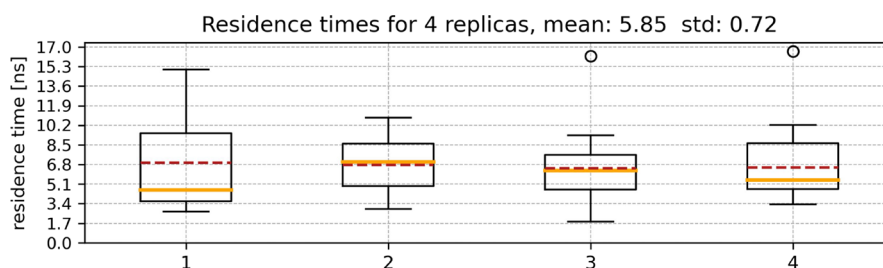
WT-MetaD replicates were performed for each trajectory with every protein−ligand complex. For each set of trajectories, the hill height of each WT-MetaD simulation was set to 1.2 kJ/mol, and different statistical analyses were performed. This resulted in 80 replicates for each complex, amounting to 720 WT-MetaD simulations across all systems. The relative residence time for each complex was measured for each of the four trajectories (Traj1−Traj4). To obtain the relative residence time, a bootstrapping procedure was performed for every CDK2−derivative complex, and the mean of all Traj1−Traj4 of each set was reported as the relative residence time.

The statistical analysis of these simulations was performed with a cumulative distribution function (CDF) where the effective relative residence time of the data according to the solid red line and the half of the trajectories where the ligand has dissociated is indicated by the red dashed line (see the Supporting Information). The τ distribution after the bootstrapping procedure agrees with the Gaussian distribution according to the black lines. The Kolmogorov−Smirnov test (KS test) shows good performance, as indicated by the distance of the Poisson cumulative distribution function when compared with an empirical CDF. Specifically, the KS test confirmed that the distribution of transition times from the simulations aligns well with the theoretical Poisson distribution, as demonstrated in Figures S2, S7, S12, S17, S21, S26, S29, S34, and S39 in the Supporting Information.

The box plot of the relative residence time for derivative D6 is shown in Figure 10. In the graph, Traj1 shows the most negligible variability with a narrow interquartile range (IQR), and tree outliers are identified at ∼5.6, ∼7.0, and ∼8.4 ns. Trajs 2 and 3 have the widest spread IQR, indicating significant variability in residence time, with only one outlier of 14 ns observed in Traj3. The Traj4 shows a moderate variability in the residence time values, with one outlier at ∼7.0 ns.

After the bootstrapping procedure, the measured $\tau_{relative}$ values for Traj1, Traj2, Traj3, and Traj4 are 3.67, 4.27, 4.81, and 3.19 ns, respectively.

The Supporting Information contains the box plots of the remaining D7 (Figure S6), D8 (Figure S11), D9 (Figure S16), roniciclib (Figure S25), D2 (Figure S28), D4 (Figure S33), and ZK304709 (Figure S38).

For derivative D7 bound to CDK2 (Figure S6), with −F at the R⁵ substituent, the measured residence times for each of Traj1−Traj4 were 3.7, 2.74, 3.13, and 3.31 ns, respectively. The final $\tau_{relative}$ after the bootstrapping procedure for all replicates was 3.2 ns, with a standard deviation of 0.36 ns. The box plot data showed only one outlier in Traj3 and two outliers in Traj4. All the box plot replicates 1−4 have a similar distribution, and no significant differences in the data are

observed. The bootstrapping procedure shows a good correspondence of the Gaussian distribution function of the data; in addition, the KS test shows a reasonable distance between the Poisson cumulative distribution function and empirical CDFs.

For derivative D8 (Figure S11) with the R⁵ substituent as the −Cl atom, the $\tau_{relative}$ of all WT-MetaD simulations were 2.95 ns for Traj1, 2.87 ns for Traj2, 3.76 ns for Traj3, and 5.15 ns for Traj4. The mean of all trajectories with 20 replicates each was 3.7 ns, with a standard deviation of 0.88 ns. In the box plot of these derivatives, three outliers were found in Traj1, Traj3, and Traj4, with a maximum outlier value of ∼18 ns in Traj4. Compared with the other sets of data, which exhibit a relatively uniform distribution, Traj4 displays a significantly higher spread of data points. Despite this nonuniformity, the KS test statistical analysis yielded positive results, indicating no statistically significant difference from the expected distribution. Furthermore, bootstrapping analysis confirmed the Gaussian-like behavior of the samples within Traj4.

The same analytical procedure was used for derivative D9 (Figure S16). For the derivative with a −Br substituent, the relative residence times for Traj1, Traj2, Traj3, and Traj4 were 5.07, 4.94, 6.15, and 4.18 ns, respectively, resulting in a mean of 5.08 ns for the four replicates. The box plot showed a more dispersed data set with a wide IQ range. Three outliers were observed in Traj2 and Traj3 and two in Traj1 and Traj4. The statistical analyses, including bootstrapping and the KS test, indicated a Gaussian distribution of the τ and the KS test value below 0.4.

For derivative D10, which has a −CF₃ substituent (Figure 11), the relative residence times measured with WT-MetaD were 4.88, 6.83, 6.22, and 5.45 ns for Traj1−Traj4, respectively, resulting in a mean of 5.85 ns with a standard deviation of 0.72 ns for all trajectories. The most considerable variability is observed in Traj1, with a wide IQR and whiskers extending up to ∼15.3 ns, indicating diverse binding events. The Traj2 and Traj4 both present moderate variability and stability, with whiskers extending to ∼11 and ∼10 ns, respectively. The Traj3 is the most stable among all trajectories analyzed, presenting a narrow IQR and whiskers of ∼8 ns, which indicates similar unbinding times for this trajectory.

The long residence time measured computationally for this derivative could be attributed to the presence of the −CF₃ substituent. This hydrophobic and bulky group might interact with binding site, altering the hydration networks around the derivative and causing local conformational adjustments, significantly impacting the binding mode and enhancing its residence time.

For the CDK2−roniciclib system (Figure S25), the relative residence times after the bootstrapping procedure were 6.5, 3.42, 5.66, and 5.44 ns for each replicate. The mean residence time across the four replicates was 5.25 ns, with a standard deviation of 1.14 ns. The box plots for roniciclib show four outliers, one in each trajectory from Traj1 to Traj4, with the maximum outlier Traj3 reaching 31.8 ns. The dispersion of the box plots indicates that trajectories 1, 3, and 2 and 4 have a similar distribution of calculated times.

The average residence time for derivative D2 bound to CDK2 (Figure S28) is 5.07 ns, with a standard deviation of 0.15 ns. In this box plot, we observed a similar median in the four replicates, with low variability and a distribution of the data symmetric along the mean. Analyzing the times measured for this compound reveals seven outliers in the data sets. Traj1, Traj2, and Traj4 have two outliers each, and Traj3 has only one outlier. However, the spread of the data and central tendency of each data set are similar and equally distributed, showing consistency between replicates. The derivative D4 bound to CDK2 (Figure S33) has a computational residence time of 6.3 ns with a standard deviation of 0.52 ns. For this compound, the times of Traj1 and Traj2 are more widely distributed across all sets, as indicated by the larger box size, and they show no outliers. Traj2 and Traj4's data distribution is narrower and similar, with two outliers of 14.4 and 12.8 ns in Traj2 and one outlier of 16.0 ns in Traj4.

ZK304709's average residence time is 4.18 ns with a standard deviation of 1.02 ns (Figure S38). This compound shows three outliers: one in Traj2 with a value of 10.1 ns and two in Traj3 with values of 13.0 and 11.7 ns. In these replicates, the residence time distribution is spread out for Traj4, while for Traj1−3, the spread of the residence time data within the boxes is quite similar.

The calculated relative residence times (τ_{calc}, in a nanosecond timescale) for all derivatives, obtained with WT-MetaD, and the corresponding τ_{exp} values are reported in Table 2. Additionally, those calculated and experimental residence
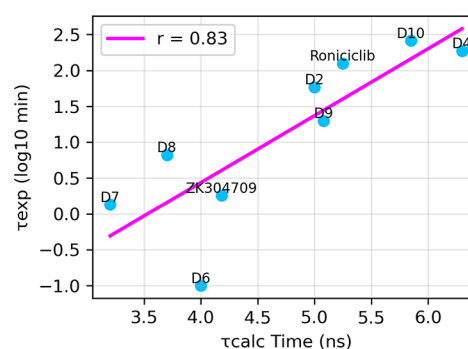

Figure 12. Regression line between the log of experimental residence time (in minutes) and computational residence times (in nanoseconds) was calculated from metadynamics for roniciclib and derivatives. The Pearson correlation coefficient (R-square) is 0.83.

Table 2. Experimental and Computational Residence Times of Derivatives[a]

derivative	substituent	τ_{exp} (min)	τ_{calc} (ns)
D6	H	0.1 ± 0.04	4.0 ± 0.6
D7	F	1.35 ± 0.63	3.2 ± 0.36
D8	Cl	6.62 ± 1.73	3.7 ± 0.88
D9	Br	19.82 ± 4.16	5.08 ± 0.68
D10	CF₃	258.65 ± 78.62	5.85 ± 0.72
roniciclib	CF₃	124.61 ± 24.11	5.25 ± 1.14
ZK304709	Br	1.81 ± 0.25	4.18 ± 1.02
D2	CF₃	58.41 ± 27.05	5.0 ± 0.15
D4	CF₃	186.31 ± 12.36	6.3 ± 0.52

[a]The table shows all derivatives with the R[5] position substitution, the τ_{exp} in a minute timescale, and τ_{calc} with metadynamics in a nanosecond timescale.

time values were compared using a regression model, where the logarithm for residence time experimental values was used. The Pearson correlation coefficient (R-square) shows a strong level of confidence, showing a value of 0.83 (Figure 12). However, the residence time calculated for derivative D6 has a value far from the tendency and does not fit well to the regression line; however, the R-square is good enough

considering the time of the experimental data and the nanosecond timescale for unbinding from metadynamics.

Clustering of Unbinding Trajectories with WT-MetaD and Interaction Fingerprints. An in-depth analysis of the dissociation trajectories for roniciclib and derivatives was performed by using a graph-based representation to visualize the unbinding trajectories. In this analysis, clusters were color-coded based on the displacement of the compounds from the active sites, and the cluster size was determined by the number of structures within each cluster. An interaction fingerprint analysis (IFP) of each compound and its clusters was performed to find the primary amino acids involved in its dissociation path.

Examining the unbinding trajectories of D6, two nodes were found near the active site, both situated less than 3Å, labeled as clusters 0 and 6 (Figure S3). These nodes initiated and transitioned to the same intermediate cluster labeled cluster 5. However, despite their common destination, the two initial nodes were not connected, reflecting different structural positions of the ligand before they left the active site. The primary transition occurred from nodes 6 to 5, continuing until the end of the dissociation trajectory at node 7. The path for derivative D6 showed a distinct dissociation route through nodes 6, 5, 3, 2, 4, and 7 as the final node, as indicated by the width of the gray arrow. Intermediate states were observed between 7 and 10 Å from the active site.

The IFP analysis reveals crucial interactions with hinge region residues such as the gatekeeper residue Phe80 in the initial clusters (Figure S4). Residues Phe82 and Leu83, part of the hinge region, form significant aromatic and hydrogen bond interactions with derivative D6; these interactions are maintained until the ligand leaves the active site and are less frequent in the final clusters 6 and 7. Another hinge region residue is His84, which interacts mainly with the ligand in the final stages of the dissociation path, as evidenced in node 7. Phe80 and Leu83 are part of the hinge region of the protein and are located in a zone with low mobility due to the importance of these residues for binding.[34] In addition, Ile10 and Val18 are located in the β-1 and β-2 segments of the protein, respectively, making aromatic interactions with derivative D6 until the final cluster 7. These residues are located in a rigid zone of the protein and form part of the active site of CDK2.[35] The analysis of the dissociation path of D6 shows that it can leave the active site by two routes, one located in β-helix D and another located by β-1,2 (Figure S5).

For derivative D7, the analysis of the dissociation path revealed a more dispersed distribution of nodes (Figure S8). Nodes 0 and 5 were situated in the bound state, with a discernible transition from node 0 to node 5. The unbinding path continued through nodes 4, 2, 3, and 1, which were located in an intermediate state before the ligand departed from the active site. Transitions with this derivative were clear, with intermediate states positioned between 6 and 10 Å. Dissociation trajectories and IFP analysis show that D7 establishes hydrogen bonds and aromatic interaction with hinge region residues Phe82, Leu83, His84, and Asp86. The interaction with these residues is less frequent in the final stages of the unbinding path, as made evident by the population of each node. Another essential residue is Ile10, part of the protein's active site and mainly forms hydrophobic interaction with the ligand until the final nodes (Figure S9). Similar to D6, the exit path of derivative D7 is through the β-helix D and β-1,2 (Figure S10).

D8 exhibited a cluster in the bound state labeled as 3, progressing through clusters 6 and 5 (Figure S13). Although cluster 0 was close to the active site, transitions from this cluster to others were less likely, as indicated by the width of the gray arrows. As the ligand passed through cluster 5, the route approached the transition state and was located between 7 and 10 Å from the active site, eventually converging to the final unbound state at node 7. The interaction fingerprints of these nodes show that the main interactions are with Phe82, Leu83, and His84, located in the hinge region. These interactions are aromatic and HB; however, the interactions with His84 are less frequent in the initial cluster close to the active site, 1−3 (Figure S14). The analysis of derivative D8 shows the tendency to leave the active site mainly through the zone of β-1,2 (Figure S15).

The derivative D9, containing the halogen −Br, displayed a more intricate dissociation pathway with widely distributed clusters (Figure S18). Nodes 1 and 3, close to the bound state, converged on node 7, progressing through intermediate states via clusters 5, 2, and 4. Cluster 0 was close to an intermediate state, and transitions from this cluster to the others were minimal. The major transition occurred between clusters in the intermediate state and unbound cluster 6. For this derivative, the main interactions with hinge region residues correspond to Phe82 and Leu83 in clusters 1−3, where the states' population is between 0.8 and 1.0. The IFP revealed that residue Ile10 makes a hydrophobic interaction with this derivative similar to the other derivatives and a high number of interactions with residues 82 to 86 at the hinge region (Figure S19). This derivative has two routes to leave the active site: one pathway close to β-1,2 and the other by the zone of the α-helix D (Figure S20).

Observing derivative D10, we found that cluster 3, which is located in the active site, was more significant compared to the same position in the other derivatives (Figure S22). This correlated with the time it took for the derivative to leave the active site. The transitions were distinct and followed a clear trend with nodes that were close and of similar size. The nodes transitioned to clusters 2 and 1 and are located approximately 10 Å away from the active site, eventually reaching node 7, where the ligand is unbound. Examination of D10 by the IFP analysis reveals aromatic and hydrophobic interactions with key residues, including Phe80, Phe82, Leu83, and His84 within the hinge region. In particular, hydrogen bonding and aromatic

interactions with residue Ile10 were consistently observed from cluster 1 to cluster 7.

Furthermore, the gatekeeper residue, Phe80, emerges as a crucial contributor in the bound state clusters, emphasizing its pivotal role in the interactions associated with this derivative (Figure S23). Derivative D10 leaves the active site through three zones compared to the two found in the other derivatives. One of these zones is α-helix D, the activation loop, and the β-1,2 motif (Figure S24).

Roniciclib exhibited a more dispersed clustering pattern than the other derivatives but showed behavior similar to that of D8 and D9 (Figure 13). Here, we show the clustering analysis for
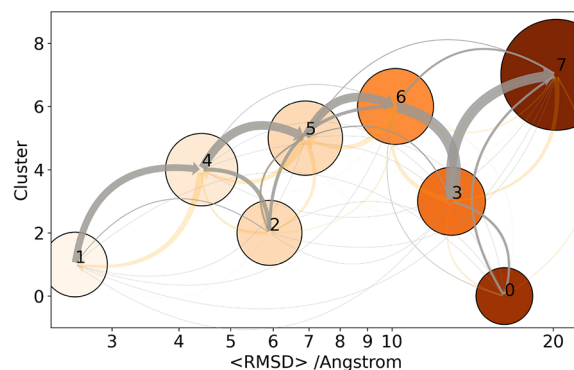

Figure 13. Clustering analysis of the four dissociation trajectories of the roniciclib/CDK2 complex. The node size represents the cluster population from 0 to 7, and the color of the nodes represents the average RMSD in the cluster, where light colors are closer to the binding site, while dark colors are farther away from the COM of the protein's active site. The distance between the nodes is on a logarithmic scale. The width of the light-orange arrows is proportional to the number of corresponding transitions between nodes, and the gray arrow is the total flow between nodes.

roniciclib as an example; the rest of the derivative cluster analyses are reported in the SI, and the 3D surface representation of the roniciclib unbinding path is shown in Figure S47. Our observation of this derivative revealed the presence of a single cluster in the bound state and three clusters located between 4 and 7 Å from the active site, spatially distributed among them. Subsequently, the dissociation pathway showed a consistent trend toward nodes 6 and 3, eventually leading to node 7. Cluster 0 was identified in the unbound state, although transitions to this node were infrequent. Notably, the IFP analysis performed on roniciclib revealed a parallel behavior with the other derivatives and residues of the hinge region, mainly featuring hydrophobic and aromatic interactions with Phe82 and Leu83. The other critical residue is Ile10, which interacts with roniciclib, forming hydrophobic interactions from the initial bound state until the ligand leaves the active site (Figure S27).

The cluster analysis for derivative D2 bound to CDK2 (Figure S30) reveals dispersed clusters between 0 and 8 Å from the COM of the protein. The clusters show a clear transition from cluster numbers 4, 6, 3, and 5, as evidenced by the gray lines that connect these clusters and their associated transitions. The spread of the clusters indicates that different metastable states are found between 0 and 8 Å. From cluster 5, the progression continues to clusters 2, 1, and 0 between 10 and 20 Å, and regardless of the cluster, all transitions lead to the final path point at cluster 7. The IFP analysis shows HB

contacts with His211 and Lys216 in the final clusters of the dissociation path (Figure S31), and derivative D2 can leave the binding site through α-helix D and β-1,2 (Figure S32).

For D4 (Figure S35), the clusters are more spread along the unbinding path, with clusters 2, 5, 3, and 7 being the most populated and showing clear progression transitions between them, as indicated by the width of the gray arrows. Cluster 7 is a crucial metastable state, and from this cluster, the unbinding path proceeds to cluster 4 and finally to cluster 6 as an exit cluster. In the dissociation path of this compound, clusters 0 and 1 are the least populated and show low transition rates to these states, as evidenced by the gray arrows. The IFP analysis (Figure S36) shows contacts with residues Phe209 and Leu210 in the initial cluster, while the final cluster exhibits HBs with Lys216 and His211. The compound leaves the binding site through the α-helix D zone and β-1,2 (Figure S37).

For ZK304709, the clusters are spread between 0 and 7 Å (Figure S40), and the ligand transitions through clusters 1, 6, and 3 with a high transition rate until reaching clusters 5 and 4. From these clusters, the ligand can proceed either to cluster 2 and then 7 or directly to cluster 7 as the final exit cluster. The IFP analysis reveals that Phe209 and Leu219 interactions are most populated in the initial cluster, while His211 interactions dominate the final clusters of the exit path (Figure S41). Like the other compounds, the ligand can leave the binding site through the α-helix D zone and β-1,2 (Figure S42).

■ MATERIALS AND METHODS

System Building and Preparation. Crystallographic structures of human CDK2 bound to roniciclib (PDB ID 5IEV), D5 (PDB ID 5IEX), and D6 (PDB ID 5IEY) were used as the initial systems. Derivatives D2, D4, D7, D8, D9, and D10 (with −F, −Cl, −Br, and −CF_3 substituents) and ZK304709 were generated with the appropriate modifications to the R^5 position of the core aminopyrimidine, D-alaninol, and sulfoximine/sulfonamide motifs from the initial roniciclib/D6/D5 X-ray crystal systems using the module "Build" from Maestro visualization software. The AMBER force field ff14SB[36] for proteins was employed to assign parameters for the CDK2 enzyme.

The hydrogen atoms for protein were added using PROPKA[37] to assign protonation states at a physiological pH of 7.0, and the hydrogen atoms for ligands were added with UCSF Chimera.[38]

The parameters for the different derivatives were obtained using Antechamber software and the General Amber Force Field (GAFF)[39] with the AM1-BCC charge scheme,[40] with a net charge of 0 for all the derivatives. The AM1-BCC method first performs an AM1 calculation to obtain Mulliken charges, followed by a bond charge correction scheme that mimics RESP charges.[39] Studies have demonstrated that AM1-BCC, when used in conjunction with the General Amber Force Field (GAFF), shows similar performance to charges derived from the HF/6-31G* level of theory, showing lower RMS deviations from experimental results in terms of atomic charges and free energy of solvation.[41]

After parametrization and molecular complex construction, all systems were solvated in a cubic box extending 16 Å from the protein. The solvation process utilized the TIP3P[42] water model, and neutralization was performed to obtain an ionic concentration of 0.15 M. The SHAKE algorithm[43] was used for bonds and a cutoff of 8.0 Å for nonbonding interactions. The long-range electrostatic interactions were treated with the Particle Mesh Ewald method (PME).[44] All molecular dynamics simulations were performed using an integration time step of 4 fs and the hydrogen mass repartition scheme.[45]

Molecular Dynamics Simulations of CDK2 Complexes. Several classical molecular dynamics simulations (cMD) for each protein−ligand complex were performed. All the cMD simulations were performed with AMBER20-GPU[46] software and using pmemd.cuda. An energetic minimization of 5000 steps of steepest descent followed by 10,000 steps of the conjugate gradient method of the complex CDK2−roniciclib and CDK2−derivatives was performed. The first minimization stage was performed to accommodate the solute, applying a restraint of 500 kcal mol^{-1} Å^{-2} on the heavy atoms of the protein. In the second stage of the minimization protocol, restraints were lowered to 100 kcal mol^{-1} Å^{-2}, and for the third stage, restraints were reduced to 1 kcal mol^{-1} Å^{-2}. In the last two stages, 1000 steps of steepest descent followed by 500 steps of the conjugate gradient method were applied. In the previous stage of the minimization protocol, all of the positional restraints were removed, and 1000 steps of steepest descent followed by 500 steps of the conjugate gradient method were performed.

After the minimization stages, a heating step was performed in the NVT ensemble using the Langevin thermostat,[47] with the temperature gradually increasing from 0 to 300 K over 1 ns. Subsequently, an equilibration stage in the NVT ensemble was carried out with a positional restraint of 50 kcal mol^{-1} Å^{-2} applied to the heavy atoms. A second equilibration stage in the NPT ensemble was performed, maintaining the temperature at 300 K and pressure at 1 atm using a Langevin thermostat and a Berendsen barostat,[47] with positional restraints of 10 kcal mol^{-1} Å^{-2} on the heavy atoms of the protein. A third equilibration simulation in NVT was conducted, adjusting the positional restraints to 2 kcal mol^{-1} Å^{-2}.

Finally, a fourth equilibration simulation was performed using an NPT ensemble without restraint. For all cMD, the SHAKE algorithm[43] was employed on all atoms covalently bonded to hydrogen atoms, and a cutoff distance of 8.0 Å for nonbonded atoms and vdW interactions was applied. The long-range electrostatic interactions were treated using the particle mesh Ewald method (PME),[44] and periodic boundary conditions were applied to avoid edge effects. All cMD simulations were performed using an integration time step of 4 fs and the hydrogen mass repartition (HMR) scheme.[45] Recent studies demonstrate that the hydrogen mass repartition (HMR) scheme and a 4 fs time step maintain simulation stability and data quality comparable to the standard 2 fs time step.[45] Works on the HEWL protein showed no stability differences between 2 and 4 fs time steps using the HMR scheme. Additionally, constant pH molecular dynamics simulations and umbrella sampling calculations at 4 fs showed minimal errors compared to 2 fs with standard masses.[48] Moreover, the HMR scheme in the CHARMM-GUI program has been validated across various systems, including lipopolysaccharides and pure membranes, showing consistent sampling with standard simulations.[49] After the equilibration stages, four independent cMD simulations of 100 ns were performed for CDK2/roniciclib and CDK2/derivatives. The final coordinates of every independent trajectory were used as input to run 20 replicates of well-tempered metadynamics (WT-MetaD) simulations. The four independent trajectories of 100 ns of the CDK2/roniciclib and CDK2/derivative systems were analyzed with AmberTools[46] and the cpptraj[50]

modules. The energetic contribution of amino acids located at 5 Å from derivatives was estimated with the LIE method[51] and MM/GBSA.[52]

Principal component analysis (PCA) was carried out on the protein structure of the simulations by using cpptraj. This analysis provided the covariance matrix and the eigenvectors of the protein. We then projected the data into three principal modes, namely, PCA1, PCA2, and PCA3. A histogram was built to represent the bin population for these modes, which allowed us to estimate the free energy from the bin population. In addition, we performed an angle analysis using two vectors. The first vector is formed by the center of mass (COM) of α carbon (CA) atoms of residues 181−198 at the α-helix segment, and the second vector is formed by the COM of CA atoms of residues 4−23 located at β-1 and β-2 segments. We measured the dot products of these two vectors throughout the simulation time of cMD using cpptraj.

Metadynamics Simulations for the Unbinding of Compounds from the CDK2 Binding Site. The metadynamics simulations were performed with AMBER20 software and run with pmemd.cuda. We patched the AMBER20 version with the Plumed v2.7.0 plugin[53] to run the metadynamics simulations.

Metadynamics simulations were performed in the NPT ensemble with the same settings previously described for the classical MDs of 100 ns. A variant of metadynamics, the well-tempered metadynamics (WT-MetaD),[30] was employed for all simulations. The WT-MetaD has been used to study the protein−ligand binding and unbinding of molecules.[54,55] Metadynamics adds an external Gaussian bias to the system to flatten the potential energy surface. The accumulation of these Gaussians in the reaction coordinate results in a flattening of the free energy surface and allows the system to overcome barriers and more easily access regions over the collective variable (CV) space, which are separated by high energy barriers, transitions, or metastable states. In WT-MetaD, the bias is added iteratively and controlled by the height of the Gaussians; this has the advantage of gradually decreasing the deposition of Gaussians and avoiding the overfilling effects compared with the classic version of metadynamics.[30] To run WT-MetaD, it is necessary to define some critical parameters, such as the height and width of the Gaussians, the bias factor, and the collective variables used to restrain the surface of potential energy that needs to be explored. The hill height was set at 1.2 kJ/mol, the stride deposition was set up to 500 steps, the width to 0.02 Å, and the bias scaling factor (γ) was set up to 12. The CV was defined as the distance between the center of mass (COM) from heavy atoms of roniciclib or the derivatives and the COM from Cα atoms of the enzyme's active sites (i.e., around 5 Å from the ligand). Roniciclib and derivatives were allowed to explore a region defined by 30 Å away from the enzyme's active site to find more possible dissociation paths. Twenty WT-MetaD replicates were generated by using the final structure from the previous 100 ns cMD simulations, totaling 80 replicates per system. The WT-MetaD simulations were stopped when compounds were located 30 Å from the binding site.

Relative Residence Time with Computational Methods. WT-MetaD simulations can provide the relative residence time, which is measured in nanoseconds. It represents the time in nanoseconds that a ligand in the bound state takes to unbind from the active site and travel 30 Å away.

For each system studied, when the ligand reached the cutoff distance of 30 Å, the WT-MetaD simulations were stopped and the time taken was considered as the unbinding time and the relative residence time. All of the replicates started and came from different seed numbers to allow randomization of the simulations.

For each of Traj1−4, a bootstrapping procedure was performed by randomly selecting 80% of the samples with replacement and performing 50,000 iterations to compute the mean relative residence time for each set of Trajs. Subsequently, Traj1−4 of each complex were depicted graphically using a box plot, and the mean residence time was determined by averaging the results from the bootstrapping of each trajectory.

The statistical analysis was performed using a Python script developed by Dr. Daria Kokh (Cancer Registry of Baden-Württemberg), accessible through GitHub (https://github.com/DKokh/tauRAMD). The metadynamics-plumed output was adapted for its use with the mentioned script.

Clustering of Unbinding Trajectories and Interaction Evaluation. To explore the interaction patterns and identify key amino acids involved in the binding of roniciclib, ZK304709, derivatives D2, D4, and D6−D10 to the CDK2 binding site, we performed an interaction fingerprint analysis using a script developed by Rebeca Wade and Dr. Doria Kokh.[56] For this analysis, we used 100 ns cMD trajectories to identify amino acids with significant contacts and specific interactions with CDK2 in the bound state for each derivative.

To investigate the dissociation pathway of roniciclib and the derivatives, we employed all dissociation trajectories from WT-MetaD to analyze interaction fingerprints (IFPs) of CDK2 bound to each compound. Specifically, we generated an IFP map based on the last 300 frames of the unbinding trajectories, we calculated the specific contacts, like hydrogen bonds, aromatics, and hydrophobic interactions, and the nonspecific contacts were considered at 4 Å from the ligand.

To cluster the dissociation trajectories of WT-MetaD, we applied the K-means algorithm to all of the dissociation trajectories. This process used eight clusters representing the dissociation paths from WT-MetaD to all derivatives and roniciclib. The resulting clusters provide insights into the unbinding trajectory path, ligand conformations, and transitions from the bound state to the dissociation path. To represent the dissociation trajectories along the exit pathway, we represent the movement of the ligand as a COM along the exit path. This was done using a homemade Python script and MDAnalysis software.[57]

■ CONCLUSIONS

In this study, we investigated the relative residence times of roniciclib and its derivatives bound to CDK2, focusing on variations at the R^5 position of sulfoximine/sulfonamides involving halogen substituents (Br, Cl, F, and CF$_3$) on the aminopyridine core of roniciclib and ZK304709. Experimental data show that changes in halogen size correlate well with changes in residence time, with larger halogen substituents increasing residence time. Computational methods, such as cMD simulations and WT-MetaD, were employed to study these differences in the compound's kinetics.

Our findings from cMD and WT-MetaD enabled us to measure and classify the residence times for various derivatives and roniciclib. These results are consistent with the experimentally reported τ values for these compounds and

allowed us to rank the derivatives according to the relative residence time while allowing characterization of the dissociation pathways using WT-MetaD. Here, we have highlighted the importance of residue Asp145 within the DFG motif, which interacts with the R^4 aminobutanol chain. Substituents at adjacent positions alter the aminobutanol configuration and affect these interactions.

In addition, the cMD trajectory analysis allowed us to measure the energetic contributions of residues located at 5 Å from the CDK2 active site for each derivative. The study performed using the LIE module shows a substantial electrostatic contribution of Asp145 to the binding of each derivative, with the energetic contribution increasing with the substituent size. For derivatives D6 and D7, the analysis shows a lower energetic contribution, with interactions mediated by hydrogen bonds (HBs) through water molecules. Derivatives D8, D9, D10, and roniciclib showed a direct HB interaction with Asp145, and the number of HBs increased with substituent size, highlighting the critical role of Asp145 in the interactions.

We also highlighted the importance of the hydration network for binding and stabilizing protein−inhibitor complexes, as evidenced by the water shell around Phe80 and Lys33. The number of water molecules around these residues decreases according to the size of the derivative, indicating a displacement of water around these residues that changes the hydration network and increases the residence time in analogs with larger sizes.

Moreover, as the substituent size increased, the angle between the C-terminal and N-terminal lobes became closed, indicating a more compact enzyme structure for more extensive derivatives, such as D10, and a more open angle for smaller ones, such as D6. When interacting with derivatives, these angle values of the protein lobes also agree with the residence time, where a complex with a sharp angle leads to a more compact structure around the derivative and can affect the residence time.

Principal component analysis (PCA) also showed that the enzyme tended to have a more compact configuration with fewer energy states for D6 and populated states with the highest free energies for D10, D2, and D4, as evidenced by bin population analysis of the structures. A similar trend is observed for derivatives D7, D8, and D9.

The relative residence times obtained from WT-MetaD using a collective variable (CV) as the reaction coordinate, represented as the distance between the center of mass (COM) of derivatives and residues within 5 Å of the active site, were in agreement with the experimental data and showed a Pearson correlation coefficient (R-square, R^2) of 0.83. Variations in the calculated residence times were observed for the derivative with the H substituent. However, the overall correlation between the experimental residence time and computational predictions was remarkable. The WT-MetaD was used to characterize the dissociation pathway of the different CDK2 inhibitors. All simulations performed with WT-MetaD show that all derivatives follow a characteristic pathway through the β-helix D and β-1 and β-2 segments of the CDK2. Computational techniques, such as cMD and WT-MetaD, helped to explain the molecular determinants that affect residence time and can provide valuable information for drug development and improvement.

■ ASSOCIATED CONTENT

ⓈⅠ Supporting Information

The Supporting Information is available free of charge at https://pubs.acs.org/doi/10.1021/acsomega.5c00555.

> Supplementary figures encompassing MMGBSA analyses of each derivative studied, raw ECDF and cumulative distribution functions of dissociation times from WT-MetaD simulations, and raw dissociation times (ns) from WT-MetaD simulations in CDK2−derivative systems; cluster and IFP analyses of the unbinding trajectories and box plots of raw dissociation times from WT-MetaD simulations on a ns timescale for all derivatives not shown in the main text; a table of contacts, a free energy landscape for each derivative, PCA and cumulative variance analyses, protein lobe angle evolution over time, and 3D representations of the unbinding paths of all studied derivatives (PDF)

■ AUTHOR INFORMATION

Corresponding Authors

Mauricio Bedoya − *Centro de Investigación de Estudios Avanzados del Maule (CIEAM), Vicerrectoría de Investigación y Postgrado and Laboratorio de Bioinformática y Química Computacional (LBQC), Departamento de Medicina Traslacional, Facultad de Medicina, Universidad Católica del Maule, Talca 3466706, Chile;* ⓘ orcid.org/0000-0002-3542-7528; Email: maurobedoyat@gmail.com

Jans Alzate-Morales − *Center for Bioinformatics, Simulation and Modeling (CBSM), Department of Bioinformatics, Faculty of Engineering, Universidad de Talca, Talca 3460000, Chile;* ⓘ orcid.org/0000-0001-9624-7849; Email: jalzate@utalca.cl

Authors

Felipe Bravo-Moraga − *Center for Bioinformatics, Simulation and Modeling (CBSM), Department of Bioinformatics, Faculty of Engineering, Universidad de Talca, Talca 3460000, Chile*

Kirill Zinovjev − *Departamento de Química Física, Universitat de Valencia, Valencia 46100, Spain;* ⓘ orcid.org/0000-0003-1052-5698

Iñaki Tuñón − *Departamento de Química Física, Universitat de Valencia, Valencia 46100, Spain;* ⓘ orcid.org/0000-0002-6995-1838

Complete contact information is available at:
https://pubs.acs.org/10.1021/acsomega.5c00555

Notes

The authors declare no competing financial interest.

■ REFERENCES

(1) Fabbro, D.; Cowan-Jacob, S. W.; Moebitz, H. Ten Things You Should Know about Protein Kinases: IUPHAR Review 14. *Br. J. Pharmacol.* **2015**, *172* (11), 2675−2700.

(2) Malumbres, M.; Barbacid, M. Cell Cycle, CDKs and Cancer: A Changing Paradigm. *Nat. Rev. Cancer* **2009**, *9* (3), 153−166.

(3) Wang, Z.; Cole, P. A. Catalytic Mechanisms and Regulation of Protein Kinases. *Methods Enzymol.* **2014**, *548*, 1−21.

(4) Akiyama, T.; Ohuchi, T.; Sumida, S.; Matsumoto, K.; Toyoshima, K. Phosphorylation of the Retinoblastoma Protein by Cdk2. *Proc. Natl. Acad. Sci. U. S. A.* **1992**, *89* (17), 7900.

(5) Fagundes, R.; Teixeira, L. K. Cyclin E/CDK2: DNA Replication, Replication Stress and Genomic Instability. *Front. Cell Dev. Biol.* **2021**, *9*, No. 774845.

(6) Malumbres, M. Cyclin-Dependent Kinases. *Genome Biol.* **2014**, *15* (6), 122.

(7) Woo, R. A.; Poon, R. Y. C. Cyclin-Dependent Kinases and S Phase Control in Mammalian Cells. *Cell Cycle* **2003**, *2* (4), 315−323.

(8) Pavletich, N. P. Mechanisms of Cyclin-Dependent Kinase Regulation: Structures of Cdks, Their Cyclin Activators, and Cip and INK4 Inhibitors. *J. Mol. Biol.* **1999**, *287* (5), 821−828.

(9) Wood, D. J.; Endicott, J. A. Structural Insights into the Functional Diversity of the CDK−Cyclin Family. *Open Biol.* **2018**, *8*, No. 180112.

(10) Vijayan, R. S. K.; He, P.; Modi, V.; Duong-Ly, K. C.; Ma, H.; Peterson, J. R.; Dunbrack, R. L., Jr.; Levy, R. M. Conformational Analysis of the DFG-Out Kinase Motif and Biochemical Profiling of Structurally Validated Type II Inhibitors. *J. Med. Chem.* **2015**, *58* (1), 466−479.

(11) Treiber, D. K.; Shah, N. P. Ins and Outs of Kinase DFG Motifs. *Chem. Biol.* **2013**, *20* (6), 745−746.

(12) Coxon, C. R.; Anscombe, E.; Harnor, S. J.; Martin, M. P.; Carbain, B.; Golding, B. T.; Hardcastle, I. R.; Harlow, L. K.; Korolchuk, S.; Matheson, C. J.; Newell, D. R.; Noble, M. E. M.; Sivaprakasam, M.; Tudhope, S. J.; Turner, D. M.; Wang, L. Z.; Wedge, S. R.; Wong, C.; Griffin, R. J.; Endicott, J. A.; Cano, C. Cyclin-Dependent Kinase (CDK) Inhibitors: Structure-Activity Relationships and Insights into the CDK-2 Selectivity of 6-Substituted 2-Arylaminopurines. *J. Med. Chem.* **2017**, *60* (5), 1746−1767.

(13) Jorda, R.; Havlíček, L.; Šturc, A.; Tušková, D.; Daumová, L.; Alam, M.; Škerlová, J.; Nekardová, M.; Peřina, M.; Pospíšil, T.; Široká, J.; Urbánek, L.; Pachl, P.; Řezáčová, P.; Strnad, M.; Klener, P.; Kryštof, V. 3,5,7-Substituted Pyrazolo[4,3-d]Pyrimidine Inhibitors of Cyclin-Dependent Kinases and Their Evaluation in Lymphoma Models. *J. Med. Chem.* **2019**, *62* (9), 4606−4623.

(14) Lücking, U.; Jautelat, R.; Krüger, M.; Brumby, T.; Lienau, P.; Schäfer, M.; Briem, H.; Schulze, J.; Hillisch, A.; Reichel, A.; Wengner, A. M.; Siemeister, G. The Lab Oddity Prevails: Discovery of Pan-CDK Inhibitor (R)-S-Cyclopropyl-S-(4-{[4-{[(1R,2R)-2-Hydroxy-1-Methylpropyl]Oxy}-5-(Trifluoromethyl)Pyrimidin-2-Yl]Amino}-phenyl)Sulfoximide (BAY 1000394) for the Treatment of Cancer. *ChemMedChem* **2013**, *8* (7), 1067−1085.

(15) Siemeister, G.; Lücking, U.; Wengner, A. M.; Lienau, P.; Steinke, W.; Schatz, C.; Mumberg, D.; Ziegelbauer, K. BAY 1000394, a Novel Cyclin-Dependent Kinase Inhibitor, with Potent Antitumor Activity in Mono- and in Combination Treatment upon Oral Application. *Mol. Cancer Ther.* **2012**, *11* (10), 2265−2273.

(16) Scholz, A.; Wagner, K.; Welzel, M.; Remlinger, F.; Wiedenmann, B.; Siemeister, G.; Rosewicz, S.; Detjen, K. M. The Oral Multitarget Tumour Growth Inhibitor, ZK 304709, Inhibits Growth of Pancreatic Neuroendocrine Tumours in an Orthotopic Mouse Model. *Gut* **2009**, *58* (2), 261−270.

(17) Siemeister, G.; Luecking, U.; Wagner, C.; Detjen, K.; Mc Coy, C.; Bosslet, K. Molecular and Pharmacodynamic Characteristics of the Novel Multi-Target Tumor Growth Inhibitor ZK 304709. *Biomed. Pharmacother. Biomedecine Pharmacother.* **2006**, *60* (6), 269−272.

(18) Ahmed, S.; Molife, R.; Shaw, H.; Steward, W.; Thomas, A.; Barrett, M.; Kowal, K.; McCoy, C.; De-Bono, J. Phase I Dose-Escalation Study of ZK 304709, an Oral Multi-Target Tumor Growth Inhibitor (MTGI), Administered for 14 Days of a 28-Day Cycle. *J. Clin. Oncol.* **2006**, *24* (18_suppl), 2076−2076.

(19) Ayaz, P.; Andres, D.; Kwiatkowski, D. A.; Kolbe, C.-C.; Lienau, P.; Siemeister, G.; Lücking, U.; Stegmann, C. M. Conformational Adaption May Explain the Slow Dissociation Kinetics of Roniciclib (BAY 1000394), a Type I CDK Inhibitor with Kinetic Selectivity for CDK2 and CDK9. *ACS Chem. Biol.* **2016**, *11* (6), 1710−1719.

(20) Bravo-Moraga, F.; Bedoya, M.; Vergara-Jaque, A.; Alzate-Morales, J. Understanding the Differences of Danusertib's Residence Time in Aurora Kinases A/B: Dissociation Paths and Key Residues Identified Using Conventional and Enhanced Molecular Dynamics Simulations. *J. Chem. Inf. Model.* **2024**, *64* (12), 4759−4772.

(21) Copeland, R. A. The Drug-Target Residence Time Model: A 10-Year Retrospective. *Nat. Rev. Drug Discovery* **2016**, *15*, 87−95.

(22) Copeland, R. A. *Evaluation of Enzyme Inhibitors in Drug Discovery. A Guide for Medicinal Chemists and Pharmacologists.*; John Wiley & Sons: **2005**; Vol. 46.

(23) Hall, R.; Dixon, T.; Dickson, A. On Calculating Free Energy Differences Using Ensembles of Transition Paths. *Front. Mol. Biosci.* **2020**, *7*, 106.

(24) Bernetti, M.; Masetti, M.; Rocchia, W.; Cavalli, A. Kinetics of Drug Binding and Residence Time. *Annu. Rev. Phys. Chem.* **2019**, *70* (1), 143−171.

(25) Callegari, D.; Lodola, A.; Pala, D.; Rivara, S.; Mor, M.; Rizzi, A.; Capelli, A. M. Metadynamics Simulations Distinguish Short- and Long-Residence-Time Inhibitors of Cyclin-Dependent Kinase 8. *J. Chem. Inf. Model.* **2017**, *57* (2), 159−169.

(26) Liang, S. S.; Liu, X. G.; Cui, Y. X.; Zhang, S. L.; Zhang, Q. G.; Chen, J. Z. Molecular Mechanism Concerning Conformational Changes of CDK2Mediated by Binding of Inhibitors Using Molecular Dynamics Simulations and Principal Component Analysis. *SAR QSAR Environ. Res.* **2021**, *32* (7), 573−594.

(27) Chen, J.; Pang, L.; Wang, W.; Wang, L.; Zhang, J. Z. H.; Zhu, T. Decoding Molecular Mechanism of Inhibitor Bindings to CDK2 Using Molecular Dynamics Simulations and Binding Free Energy Calculations. *J. Biomol. Struct. Dyn.* **2020**, *38* (4), 985−996.

(28) Zuo, K.; Kranjc, A.; Capelli, R.; Rossetti, G.; Nechushtai, R.; Carloni, P. Metadynamics Simulations of Ligands Binding to Protein Surfaces: A Novel Tool for Rational Drug Design. *Phys. Chem. Chem. Phys.* **2023**, *25* (20), 13819−13824.

(29) Galvani, F.; Pala, D.; Cuzzolin, A.; Scalvini, L.; Lodola, A.; Mor, M.; Rizzi, A. Unbinding Kinetics of Muscarinic M3 Receptor Antagonists Explained by Metadynamics Simulations. *J. Chem. Inf. Model.* **2023**, *63* (9), 2842−2856.

(30) Barducci, A.; Bussi, G.; Parrinello, M. Well-Tempered Metadynamics: A Smoothly Converging and Tunable Free-Energy Method. *Phys. Rev. Lett.* **2008**, *100* (2), No. 020603.

(31) Abrams, C.; Bussi, G. Enhanced Sampling in Molecular Dynamics Using Metadynamics, Replica-Exchange, and Temperature-Acceleration. *Entropy* **2014**, *16* (1), 163−199.

(32) Abel, R.; Wang, L.; Harder, E. D.; Berne, B. J.; Friesner, R. A. Advancing Drug Discovery through Enhanced Free Energy Calculations. *Acc. Chem. Res.* **2017**, *50* (7), 1625−1632.

(33) Bernardi, R. C.; Melo, M. C. R.; Schulten, K. Enhanced Sampling Techniques in Molecular Dynamics Simulations of Biological Systems. *Biochim. Biophys. Acta BBA - Gen. Subj.* **2015**, *1850* (5), 872−877.

(34) Otyepka, M.; Bártová, I.; Kříž, Z.; Koča, J. Different Mechanisms of CDK5 and CDK2 Activation as Revealed by CDK5/P25 and CDK2/Cyclin A Dynamics*. *J. Biol. Chem.* **2006**, *281* (11), 7271−7281.

(35) Bártová, I.; Koča, J.; Otyepka, M. Functional Flexibility of Human Cyclin-Dependent Kinase-2 and Its Evolutionary Conservation. *Protein Sci. Publ. Protein Soc.* **2008**, *17* (1), 22−33.

(36) Case, D. A.; Ben-Shalom, I. Y.; Brozell, S. R.; Cerutti, D. S.; Cheatham, T. E. III; Cruzeiro, V. W. D.; Darden, T. A.; Duke, R. E.; Ghoreishi, D.; Gilson, M. K.et al.*AMBER 2018*; University of California: San Francisco, 2018.

(37) Olsson, M. H. M.; Søndergaard, C. R.; Rostkowski, M.; Jensen, J. H. PROPKA3: Consistent Treatment of Internal and Surface Residues in Empirical pKa Predictions. *J. Chem. Theory Comput.* **2011**, *7* (2), 525−537.

(38) Pettersen, E. F.; Goddard, T. D.; Huang, C. C.; Couch, G. S.; Greenblatt, D. M.; Meng, E. C.; Ferrin, T. E. UCSF Chimera−a

Visualization System for Exploratory Research and Analysis. *J. Comput. Chem.* **2004**, *25* (13), 1605−1612.

(39) Wang, J.; Wolf, R. M.; Caldwell, J. W.; Kollman, P. A.; Case, D. A. Development and Testing of a General Amber Force Field. *J. Comput. Chem.* **2004**, *25* (9), 1157−1174.

(40) Jakalian, A.; Bush, B. L.; Jack, D. B.; Bayly, C. I. Fast, Efficient Generation of High-Quality Atomic Charges. AM1-BCC Model: I. Method. *J. Comput. Chem.* **2000**, *21* (2), 132−146.

(41) Jakalian, A.; Jack, D. B.; Bayly, C. I. Fast, efficient generation of high-quality atomic charges. AM1-BCC model: II. Parameterization and validation. *J. Comput. Chem.* **2002**, *23* (16), 1623−1641.

(42) Price, D. J.; Brooks, C. L. A Modified TIP3P Water Potential for Simulation with Ewald Summation. *J. Chem. Phys.* **2004**, *121* (20), 10096−10103.

(43) Ryckaert, J.-P.; Ciccotti, G.; Berendsen, H. J. C. Numerical Integration of the Cartesian Equations of Motion of a System with Constraints: Molecular Dynamics of n-Alkanes. *J. Comput. Phys.* **1977**, *23* (3), 327−341.

(44) Essmann, U.; Perera, L.; Berkowitz, M. L.; Darden, T.; Lee, H.; Pedersen, L. G. A Smooth Particle Mesh Ewald Method. *J. Chem. Phys.* **1995**, *103* (19), 8577−8593.

(45) Hopkins, C. W.; Le Grand, S.; Walker, R. C.; Roitberg, A. E. Long-Time-Step Molecular Dynamics through Hydrogen Mass Repartitioning. *J. Chem. Theory Comput.* **2015**, *11* (4), 1864−1874.

(46) Case, D. A.; Cheatham, T. E.; Darden, T.; Gohlke, H.; Luo, R.; Merz, K. M.; Onufriev, A.; Simmerling, C.; Wang, B.; Woods, R. J. The Amber Biomolecular Simulation Programs. *J. Comput. Chem.* **2005**, *26* (16), 1668−1688.

(47) Berendsen, H. J. C.; Postma, J. P. M.; van Gunsteren, W. F.; DiNola, A.; Haak, J. R. Molecular Dynamics with Coupling to an External Bath. *J. Chem. Phys.* **1984**, *81* (8), 3684−3690.

(48) Jung, J.; Kasahara, K.; Kobayashi, C.; Oshima, H.; Mori, T.; Sugita, Y. Optimized Hydrogen Mass Repartitioning Scheme Combined with Accurate Temperature/Pressure Evaluations for Thermodynamic and Kinetic Properties of Biological Systems. *J. Chem. Theory Comput.* **2021**, *17* (8), 5312−5321.

(49) Gao, Y.; Lee, J.; Smith, I. P. S.; Lee, H.; Kim, S.; Qi, Y.; Klauda, J. B.; Widmalm, G.; Khalid, S.; Im, W. CHARMM-GUI Supports Hydrogen Mass Repartitioning and Different Protonation States of Phosphates in Lipopolysaccharides. *J. Chem. Inf. Model.* **2021**, *61* (2), 831−839.

(50) Roe, D. R.; Cheatham, T. E. PTRAJ and CPPTRAJ: Software for Processing and Analysis of Molecular Dynamics Trajectory Data. *J. Chem. Theory Comput.* **2013**, *9* (7), 3084−3095.

(51) Aqvist, J.; Medina, C.; Samuelsson, J. E. A New Method for Predicting Binding Affinity in Computer-Aided Drug Design. *Protein Eng.* **1994**, *7* (3), 385−391.

(52) Genheden, S.; Ryde, U. The MM/PBSA and MM/GBSA Methods to Estimate Ligand-Binding Affinities. *Expert Opin. Drug Discovery* **2015**, *10* (5), 449−461.

(53) Bonomi, M.; Branduardi, D.; Bussi, G.; Camilloni, C.; Provasi, D.; Raiteri, P.; Donadio, D.; Marinelli, F.; Pietrucci, F.; Broglia, R. A.; Parrinello, M. PLUMED: A Portable Plugin for Free-Energy Calculations with Molecular Dynamics. *Comput. Phys. Commun.* **2009**, *180* (10), 1961−1972.

(54) Limongelli, V.; Bonomi, M.; Marinelli, L.; Gervasio, F. L.; Cavalli, A.; Novellino, E.; Parrinello, M. Molecular Basis of Cyclooxygenase Enzymes (COXs) Selective Inhibition. *Proc. Natl. Acad. Sci. U. S. A.* **2010**, *107* (12), 5411−5416.

(55) Bešker, N.; Gervasio, F. L. Using Metadynamics and Path Collective Variables to Study Ligand Binding and Induced Conformational Transitions. In *Computational Drug Discovery and Design*; Baron, R., Ed.; Methods in Molecular Biology; Springer New York: New York, NY, 2012; Vol. *819*, pp 501−513. .

(56) Kokh, D. B.; Doser, B.; Richter, S.; Ormersbach, F.; Cheng, X.; Wade, R. C. A Workflow for Exploring Ligand Dissociation from a Macromolecule: Efficient Random Acceleration Molecular Dynamics Simulation and Interaction Fingerprint Analysis of Ligand Trajectories. *J. Chem. Phys.* **2020**, *153* (12), No. 125102.

(57) Michaud-Agrawal, N.; Denning, E. J.; Woolf, T. B.; Beckstein, O. MDAnalysis: A Toolkit for the Analysis of Molecular Dynamics Simulations. *J. Comput. Chem.* **2011**, *32* (10), 2319−2327.